PAPER

A novel hydrogenic spectroscopic technique for inferring the role of plasma–molecule interaction on power and particle balance during detached conditions

To cite this article: K Verhaegh *et al* 2021 *Plasma Phys. Control. Fusion* **63** 035018

View the article online for updates and enhancements.

A novel hydrogenic spectroscopic technique for inferring the role of plasma–molecule interaction on power and particle balance during detached conditions

K Verhaegh[1,2,3] , B Lipschultz[2] , C Bowman[2] , B P Duval[3], U Fantz[4,5] , A Fil[1,2] ,
J R Harrison[1] , D Moulton[1], O Myatra[2], D Wünderlich[4] , F Federici[2], D S Gahle[1,6] ,
A Perek[7] , M Wensing[3] , the TCV Team[8] and the EuroFusion MST1 Team[9]

[1] Culham Centre for Fusion Energy, Culham, United Kingdom
[2] York Plasma Institute, University of York, York, United Kingdom
[3] École Polytechnique Fédérale de Lausanne (EPFL), Swiss Plasma Center (SPC), CH-1015 Lausanne,
Switzerland
[4] Max Planck Institute for Plasma Physics, Garching bei München, Germany
[5] Augsburg University, Augsburg, Germany
[6] SUPA, University of Strathclyde, Glasgow, United Kingdom
[7] DIFFER, Eindhoven, The Netherlands

E-mail: kevin.verhaegh@ukaea.uk

CrossMark

Abstract
Detachment, an important mechanism for reducing target heat deposition, is achieved through
reductions in power, particle and momentum; which are induced through plasma–atom and
plasma–molecule interactions. Experimental research in how those reactions precisely
contribute to detachment is limited. Both plasma–atom as well as plasma–molecule interactions
can result in excited hydrogen atoms which emit atomic line emission. In this work, we
investigate a new Balmer Spectroscopy technique for Plasma–Molecule Interaction—BaSPMI.
This first disentangles the Balmer line emission from the various plasma–atom and
plasma–molecule interactions and secondly quantifies their contributions to particle (ionisation
and recombination) and power balance (radiative power losses). Its performance is verified
using synthetic diagnostic techniques of both attached and detached TCV and MAST-U
SOLPS-ITER simulations. We find that H_2 plasma chemistry involving H_2^+ and/or H^- can
substantially elevate the $H\alpha$ emission during detachment, which we show is an important
precursor for Molecular Activated Recombination. An example illustration analysis of the full
BaSPMI technique shows that the hydrogenic line series, even $Ly\alpha$ as well as the medium-n
Balmer lines, can be significantly influenced by plasma–molecule interactions by tens of

---

[8] See author list of 'S Coda *et al* 2019 *Nucl. Fusion* **59** 112023'.
[9] See author list of 'B Labit *et al* 2019 *Nucl. Fusion* **59** 086020'.

percent. That has important implications for using atomic hydrogen spectroscopy for diagnosing divertor plasmas.

(Some figures may appear in colour only in the online journal)

1. Introduction

Divertor detachment is predicted to be crucial for handling the power exhaust of future fusion devices, such as ITER [1–3]. Divertor detachment implies a simultaneous reduction of the target plasma temperature, target ion flux and the target pressure. This is achieved through atomic and molecular processes driving power losses, momentum losses and particle losses (through a reduction of ion sources and/or increases of ion sinks). All three losses play an important role in the detached state and require detailed characterisation [4–6].

The hydrogenic line series (such as the Balmer line series) has been routinely monitored in tokamaks using both line of sight spectroscopy as well as filtered camera imaging systems. Those measurements can be used to study some of the plasma–atom interactions involved in detachment. First, this involved studying the increase of the electron-ion recombination (EIR) ion sink during detachment [7–9]. Later studies involved estimating ion sources [5, 10, 11], as well as the power lost due to ionisation [10].

Plasma–molecule interactions involve both *collisions* and *reactions* which impact power, particle and momentum balance. H_2 becomes rovibronically (e.g. rotationally, vibrationally and electronically) excited through *collisions* between the electrons and H_2 [12–19]. De-excitation of electronically excited molecules can result in H_2 Fulcher band emission. Vibrationally excited molecules strongly promote the creation of H^- and H_2^+ (for T_e between 1 and 4 eV). H_2^+ and H^- can undergo *reactions* with the plasma resulting in molecular activated recombination (MAR) and molecular activated ionisation (MAI) ion sinks/sources [6, 15, 18, 20, 21].

Experimental investigations on plasma–molecule interactions in tokamak divertors are, in general, few and are typically based on measuring the H_2 Fulcher band spectra [13, 14, 16, 17]. Such measurements provide useful information on the rovibrational structure of H_2 [13] and thus provide *direct* evidence of plasma-molecule *collisions* as the molecules get rovibronically excited by the plasma. It can also provide H_2 dissociation estimates [16]. Models can be used to *extrapolate* those Fulcher band measurements (from plasma-molecule *collisions* resulting in excited molecules) to MAR/MAI plasma-molecule *reaction* estimates [13], on which the Fulcher band provides no *direct* information. The H_2 Fulcher band is however complicated to diagnose given its limited brightness and that measuring it fully requires a relative wide wavelength (590–640 nm) range as well as a relatively high spectral resolution [13] to resolve its band structure.

H^- and H_2^+ undergo reactions with the plasma leading to MAR or MAI, which can also lead to *excited atoms* modifying the hydrogenic line series emission [13–15, 21, 22], particularly $H\alpha$ and $H\beta$. Such molecule-derived modifications to the Balmer line series and their associated radiative losses have not yet been studied experimentally before in tokamak divertors and provide an alternative way of estimating MAR/MAI as well as atomic line radiation related to H_2 plasma chemistry.

1.1. This work and its outline

In this work, we describe an analysis technique which can quantify the contributions of plasma–molecule interactions to the Balmer line emission and use that to estimate the role plasma–molecule interactions play on particle and power balance during detachment. Our technique—Balmer spectroscopy plasma–molecule interaction (BaSPMI) is explained in section 2. BaSPMI first executes the technique previously developed by the authors [10, 9] to separate the *atomic* process contributions (electron-impact excitation and EIR) from the analysis of medium-n ($n = 5, 6, 7$) Balmer lines (section 2.1). $H\alpha$ and $H\beta$ emission is generally more sensitive to plasma–molecule interactions than the medium-n Balmer lines. We extrapolate the *atomic process information* from the *medium-n Balmer lines* to $H\alpha$ and $H\beta$. We compare this to the measured $H\alpha$ and $H\beta$ to estimate the contribution of excited atoms related to H_2 plasma chemistry to $H\alpha$ and $H\beta$ (section 2.2). Using collisional-radiative model results from Yacora (on the Web) [22, 23], Balmer line emission attributed to H_2 plasma chemistry involving H_2^+, H^- is quantitatively separated using the ratio of the sum of the molecular process contributions of $H\alpha$ and $H\beta$ (section 2.3). Those contributions are then used individually to:

- Estimate Molecular Activated ion sinks (Recombination)/sources (Ionisation)–MAR/MAI for each emission channel (section 2.5.2).
- Estimate the contribution of plasma–molecule interactions to:
  * the entire hydrogenic spectra providing radiative loss estimates for excited atoms arising from plasma interactions with H_2, H_2^+ and H^- (section 2.5.1).
  * the medium-n Balmer lines, which is accounted for self-consistently (section 2.4).

The applicability of this technique is verified using synthetic diagnostic data from TCV and MAST-U SOLPS

simulations in section 3. Here the analysis estimates, based on a synthetic spectrometer signal analysed through BaSPMI, are compared against the values directly obtained from the simulation. The performance of the technique is further tested by artificially removing emission process contributions from the synthetic spectrometer signals and checking the analysis response (section 3.3). We find that the analysis behaves as expected: the synthetic diagnostic analysis estimates are in quantitative agreement (within uncertainty) with the direct values obtained from the simulation.

BaSPMI has been applied to a set of TCV experimental data, which is presented in [24]. For a complete picture of BaSPMI we have also included a brief example of the TCV experimental data analysis in this paper in section 4. This shows the capabilities of BaSPMI to separate various hydrogen emission lines in its different emission pathways (e.g. EIR (of H^+), electron-impact excitation (of H) and related to H_2 plasma chemistry (involving H_2, H_2^+ and H^-).

We further discuss the Balmer line emission associated with H_2 (as opposed to H_2^+ and H^-) in section 5.1, which we show is expected to be negligible in the discussed detached divertor conditions. As the analysis relies on the fact that H_2 plasma chemistry results in additional $H\alpha$ emission, other processes which could result in additional $H\alpha$ emission may interfere with this analysis. These other contributions are discussed and estimated in section 5.2. We discuss how using this analysis for MAR/MAI estimates compares against using model extrapolations from the H_2 Fulcher band measurements in section 5.4. The dependence of this analysis chain on molecular data is further discussed in section 5.5. The application of BaSPMI to more reactor-like tokamak environments is discussed in section 5.6, together with analysis enhancement suggestions.

The development of BaSPMI was motivated by observing that the 'atomic extrapolated $H\alpha$' bifurcates from the measured $H\alpha$ at the detachment onset [25]. Our theoretical analysis indicates that this bifurcation is a particularly powerful indicator for plasma–molecule interactions. This is in agreement with the application of the *full BaSPMI analysis* on experimental TCV data in [24], where this bifurcation is shown to correspond to the onset of MAR as well as Balmer line emission related to H_2^+ chemistry. In this work we show that this bifurcation can be used for *quantitative* MAR estimates, which are in agreement with those from the full BaSPMI analysis (section 5.3). The full self-consistent analysis chain BaSPMI is, however, required for estimating the impact of H_2 plasma chemistry on the total hydrogenic spectra which can be important for ionisation source estimates as highlighted in [24].

H_2 plasma chemistry involves reactions which can result in excited atoms and thus atomic line emission. It is important to account for this when analysing the hydrogenic Balmer line series. This work provides an analysis technique—BaSPMI to dissect the hydrogen Balmer line emission into its various components and use this to perform a power and particle balance analysis accounting for both plasma–atom interactions as well as plasma–molecule interactions.
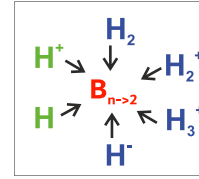

Figure 1. Schematic overview of the various reaction channels resulting in hydrogenic atomic Balmer line emission, adopted from [22]. Blue indicates contributions related to H_2 plasma chemistry, green indicates purely 'atomic' interactions and red indicates the total emission.

2. Spectral analysis techniques of inferring information on plasma–molecule interaction from the Balmer spectra

The goal of our analysis technique BaSPMI is to quantify the contribution of plasma–molecule interactions to $H\alpha$[10] and use this to provide quantitative estimates on the influence of molecules on power losses; particle (ion) sources/sinks and Balmer line emission. A schematic overview of the contribution of the various plasma–atom and plasma–molecule interactions to excited hydrogen neutrals (which emit hydrogenic line emission) are shown in figure 1.

The analysis developed in this work builds upon the Balmer line analysis techniques developed previously by the authors in [10], of which we provide a summary in section 2.1. For the analysis we utilise the measurements of $H\alpha$, $H\beta$ in addition to two medium-n Balmer lines ($n = 5,6,7$) [10]. The analysis works on the basis of assigning all *measured* Balmer line emission to the sum of (1) the *expected* Balmer line emission from plasma–atom interactions (involving H, H^+) and (2) H_2 plasma chemistry related contributions (involving H_2, H_2^+, H^-). Contributions from H_3^+ are ignored since our post-processing (in section 3) indicates that its contribution to the Balmer line emission is negligible ($\ll 0.1\%$). A flowchart of the analysis scheme is provided in figure 2 and consists of several steps.

(a) We apply the analysis technique from [10] on the medium-n Balmer lines, *which considers only atomic processes* (e.g. electron-impact excitation of H and EIR of H^+). Initially we attribute all medium-n Balmer line emission to only atomic processes. The analysis from [10] consists of several sub-steps and more information can be found in section 2.1:

1. We infer the electron density from the Balmer line shape through Stark broadening [10, 25].
2. The fraction of the medium-n Balmer line ratio due to electron-impact excitation $F_{exc}(n)$ and EIR $F_{rec}(n) = 1 - F_{exc}(n)$ is determined from the ratio of two medium-n Balmer lines. This uses an assumed possible range of neutral fractions n_o/n_e.

---

[10] In this work we denote H as hydrogen since most of the atomic/molecular data is available for hydrogen. In experiments, however, generally deuterium is used—more information can be found in section 5.5.
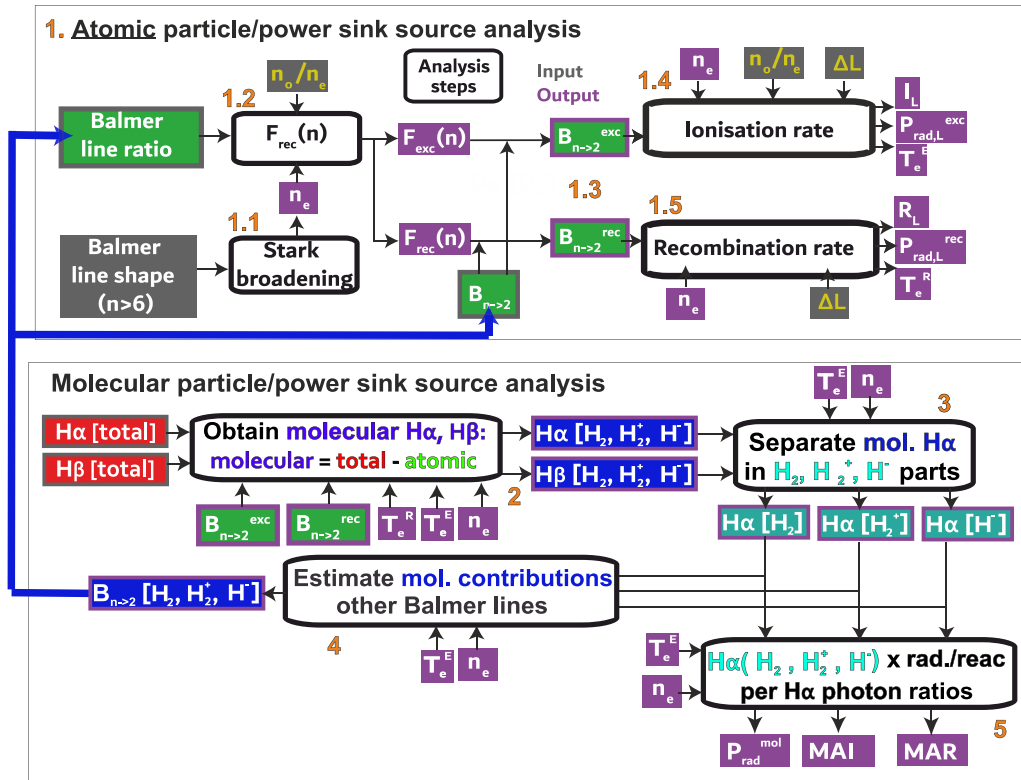
Figure 2. Schematic overview of the full analysis routine. The atomic analysis part has been adopted from [10]. The orange numbers indicate the sequence of the various steps. The nomenclature used is adopted from [10]: n_o/n_e—neutral fraction; ΔL—emission pathlength; n_e—electron density (from Stark broadening [10]); T_e^E—estimated electron temperature in the excitation region; T_e^R—estimated electron temperature in the recombination region; $B_{n\rightarrow2}^{exc}$—atomic Balmer line emission due to excitation; $B_{n\rightarrow2}^{rec}$—atomic Balmer line emission due to recombination. The steps within the blocks 'Obtain molecular $H\alpha$'; 'Separate mol. $H\alpha$'; 'Estimate mol. contributions'; '$H\alpha(H_2, H_2^+, H^-)$ x rad./reac per $H\alpha$ photon ratios' are shown in more detailed in figures 3, 4, 6 and 7 respectively.

3. These fractions are multiplied with the measured medium-n Balmer line brightness to obtain the Balmer line brightnesses due to electron-impact excitation ($B_{n\rightarrow2}^{exc}$) and EIR ($B_{n\rightarrow2}^{rec}$).

4. The (line-integrated) ionisation rate I_L, radiative power loss due to electron-impact excitation $P_{rad,L}^{exc}$ and respective excitation region temperature T_e^E is estimated from $B_{n\rightarrow2}^{exc}$ using an assumed range of possible neutral fractions n_o/n_e and pathlengths ΔL.

5. The (line-integrated) recombination rate R_L, radiative power loss due to EIR $P_{rad,L}^{rec}$ and respective recombination region temperature T_e^R is estimated from $B_{n\rightarrow2}^{rec}$ using an assumed range of possible pathlengths ΔL.

(b) The *sum of the contributions* of H_2 plasma chemistry (involving H_2, H_2^+ and H^-) to $H\alpha$ and $H\beta$ are estimated using the measured $H\alpha, H\beta$ brightnesses and outputs from the 'atomic particle/power sink/source analysis' as will be explained in section 2.2.

(c) The *individual contributions* (H_2, H_2^+ and H^-) of plasma-chemistry to $H\alpha$ are *separated* using the ratio between the sum of those contributions to $H\alpha$ and $H\beta$ as will be explained in section 2.3.

(d) The individual contributions of H_2 plasma-chemistry to $H\alpha$ are used to estimate the individual contributions of H_2 plasma-chemistry to the medium-n Balmer line as will

be explained in section 2.4. This information is used to modify the atomic process contributions to the medium-n Balmer line brightnesses in step 1, which is then iterated up until step 4 until a converged result is obtained.

(e) After a converged result is obtained, the individual contributions of $H\alpha$ associated with H_2 plasma-chemistry are used to estimate (line-integrated) MAI ion sources, MAR ion sinks as well as the (line-integrated) radiated power due to excited atoms after plasma-molecule reactions involving H_2, H_2^+ and H^-—$P_{rad,L}^{mol}$. This will be explained in sections 2.5.1 and 2.5.2.

There are two different versions of the analysis we can apply, ranging in complexity: (1) a 'simple' version: include only 'atomic' emission channels for the medium-n Balmer lines (e.g. no iteration applied) and optionally estimate the molecular component of $H\alpha$ and assume this is purely due to H_2^+ to obtain MAR/MAI/radiative loss rates (see section 5.3); (2) the complex 'full' version, which does apply the iterative technique and separates $H\alpha$ into its H_2, H_2^+, H^- contributions. We have applied the 'full' version to the results unless otherwise specified.

We summarise the reactions on which BaSPMI provides estimates, in terms of radiative loss and particle sinks/sources in table 1. Note that this table is not an overview of all the

Table 1. Overview of the various reactions on which the analysis provides information in terms of particle (H^+ ion) balance (bal.) and radiative power loss (radiation). If the analysis provides information on it, it is denoted with a '✓' (whereas N/A implies not applicable). MAR/MAI/MAD mean Molecular Activated Recombination/Ionisation/Dissociation.

Reactions	Ion bal.	Emission	Comment
$e^- + H \rightarrow e^- + H$	N/A	✓	Electron impact excitation (of H)
$e^- + H \rightarrow 2e^- + H^+$	✓	N/A	Ionisation
$e^- + H^+ \rightarrow H$	✓	✓	(Radiative) Electron-Ion Recombination (of H^+)—EIR
$2e^- + H^+ \rightarrow e^- + H$	✓	✓	(Three body) Electron-Ion Recombination (of H^+)—EIR
$e^- + H_2 \rightarrow e^- + H + H$	N/A	✓	Dissociation
$e^- + H_2 \rightarrow 2e^- + H + H^+$	✓	✓	Electron impact dissociative ionisation (part of MAI chain)
$e^- + H_2^+ \rightarrow 2e^- + H^+ + H^+$	✓	N/A	Electron impact dissociative ionisation (part of MAI chain)
$e^- + H_2^+ \rightarrow H + H^+ + e^-$	N/A	✓	Dissociation (part of MAD (or MAI[a]) chain)
$e^- + H_2^+ \rightarrow H + H$	✓	✓	Dissociative recombination (part of MAR (or MAD[a]) chain)
$H^+ + H^- \rightarrow H + H^+ + e^-$	N/A	✓	Proton impact ionisation (part of MAD chain)
$H^+ + H^- \rightarrow H + H$	✓	✓	Mutual neutralisation (part of MAR chain)

[a] Whether interactions with H_2^+ are part of a MAR, MAD or MAI chain depends on the reaction process which *created* H_2^+ (e.g. whether it is molecular charge exchange $H^+ + H_2 \rightarrow H_2^+ + H$ or H_2 ionisation $e^- + H_2 \rightarrow 2e^- + H_2^+$). This is explained in section 2.5.2.

important plasma–molecule interactions. Most notably, the table does not contain the reactions where H_2^+ & H^- are being 'created' as these do not directly lead to Balmer line emission (but the destruction of these species, as shown in table 1, does).

2.1. Atomic Balmer line analysis and analysis framework

The basic steps of the atomic Balmer line analysis technique of the upper block of figure 2 were discussed above and some important additional details are discussed below here. More information can be found in [10].

In this analysis the emission is modelled using a collisional-radiative model by a 0D 'semi slab-like' plasma model. Here the emission region has a pathlength (e.g. width) ΔL, and an electron density n_e, while a different temperature is ascribed to the electron-impact excitation (of H)—T_e^E and EIR (of H^+)—T_e^R regions (essentially a 'dual slab' model). For simplicity, this model assumes that the H^+ density equals the electron density ($n_{H^+} = n_e$, ignoring impurities); which is expected to have a negligible impact [9, 10, 25] on this analysis. The emission for the excitation/recombination region is determined using results from collisional radiative modelling from ADAS [26, 27] in the form of photon emission coefficients (PECs—photons m^3 s^{-1}). The PEC is defined as the population coefficient ($\frac{n_p}{n_e n_0}$ where n_p is the population density of the p state and $n_0 = \sum_p n_p$ is the total density of the emitter (sum of the population densities)) multiplied with the respective Einstein coefficient A_{pq} for a $p \rightarrow q$ transition: $PEC(p,q) = A_{pq}\frac{n_p}{n_e n_0}$ [26, 27].

All the analysis shown in this work is done in a 'probabilistic' manner, which is also employed for all plasma–molecule interaction related estimates [10]. For *each* input parameter in figure 2, depending on their uncertainty, a 'probability density function' (PDF) is ascribed. The peak of this parameter corresponds to the measured input parameter, whereas its width and shape corresponds to the expected uncertainty of this parameter. According to those PDFs, samples of input values for each parameter in figure 2 are obtained through Monte Carlo sampling. These are then propagated to the output parameters,
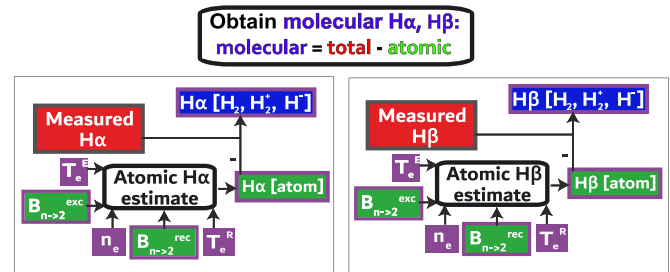

Figure 3. Schematic analysis flow chart for separating the atomic and molecular contributions from the $H\alpha$ and $H\beta$ emission. This represents step 2 'Obtain molecular $H\alpha, H\beta$' in figure 2.

yielding a PDF for the output parameters from which the estimates and their uncertainties are obtained.

The full atomic & molecular analysis requires implementing $H\alpha$ & $H\beta$ brightnesses in addition to the two medium-n Balmer lines used in the atomic analysis in [10]. This required modification to the PDF description of the relative brightnesses with respect to [10], which has to be similar for all possible line ratios. This was achieved using multivariate normal distributions with a set correlation strength according to [28]; which leads to normal distributions for all the various line ratios ($\sigma = 0.075$) as well as the line intensities ($\sigma = 0.15$) [28]. In addition to [10], we have also included random, uncorrelated, uncertainties in both the atomic and molecular collisional radiative model coefficients (e.g. PECs and reaction rates from ADAS [26, 27], Yacora [22, 23] and AMJUEL [29–31]); which are parameterized by uniform PDFs. For the atomic rates/emission coefficients an uncertainty of 12.5% is assumed; while this is assumed to be 25% for the molecular related coefficients.

2.2. Inferring molecular contributions to Hα emission

After the medium-n Balmer lines are analysed from the viewpoint of 'atomic' interactions, those results are used with measured $H\alpha, H\beta$ brightnesses to estimate the contribution of
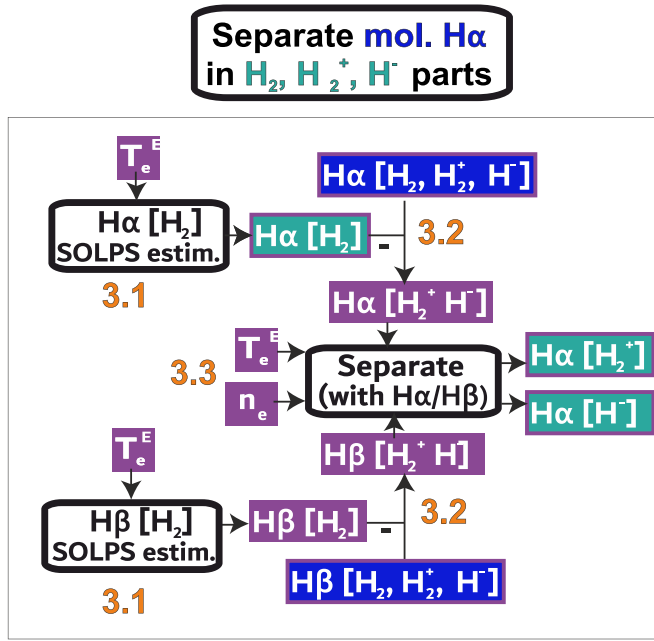
Figure 4. Schematic analysis flow chart for separating the various pathways of the molecular $H\alpha$ emission. This represents step 3 'Separate mol.$H\alpha$ in H_2, H_2^+, H^- parts' in figure 2.

H_2 plasma chemistry to $H\alpha$ and $H\beta$, which is illustrated in figure 3, which is step 2 in figure 2.

This is achieved by assuming that the *total measured $H\alpha$*, $H\beta$ ($B_{3,4\rightarrow2}^{total}$) equals its *atomic part* ($B_{3,4\rightarrow2}^{atom}$) plus its *molecular part* ($B_{3,4\rightarrow2}^{H_2,H_2^+,H^-}$)—as shown in equation (1). That assumption is further discussed for TCV in section 5.2.

$$B_{3,4\rightarrow2}^{H_2,H_2^+,H^-} = B_{3,4\rightarrow2}^{\text{tot,measured}} - B_{3,4\rightarrow2}^{\text{atom}}. \tag{1}$$

The output information from the *atomic* analysis of the medium-n Balmer lines (figure 2) is utilised to *extrapolate* the *atomic parts* of the medium-n Balmer line brightnesses of a Balmer line (typically $n = 5, 6, 7$) to $H\alpha$ and $H\beta$, yielding the *atomic parts* of the $H\alpha$ and $H\beta$ brightnesses. Utilising the recombination/excitation inferred temperatures (T_e^E, T_e^R) and the Stark inferred density (n_e), the individual excitation ($B_{n\rightarrow2}^{exc}$) and recombination ($B_{n\rightarrow2}^{rec}$) medium-n Balmer line brightnesses are extrapolated to $H\alpha$ and $H\beta$ ($B_{3,4\rightarrow2}^{atom,extrapolated}$) as shown in equation (2) and schematically in figure 3, [10].

$$B_{3,4\rightarrow2}^{atom,extrapolated} = B_{n\rightarrow2}^{exc} \frac{PEC_{3,4\rightarrow2}^{exc}(n_e, T_e^E)}{PEC_{n\rightarrow2}^{exc}(n_e, T_e^E)} + B_{n\rightarrow2}^{rec} \frac{PEC_{3,4\rightarrow2}^{rec}(n_e, T_e^R)}{PEC_{n\rightarrow2}^{rec}(n_e, T_e^R)}. \tag{2}$$

The extrapolated 'atomic' contribution to $H\alpha$ and $H\beta$ is then subtracted from the total measured $H\alpha$ and $H\beta$ brightnesses (equation (1), figure 3) to estimate the $H\alpha$ and $H\beta$ brightnesses associated with H_2 plasma.

2.3. Separating multiple molecular contributions to $H\alpha$ emission

Now that we obtained an estimate for $B_{3,4\rightarrow2}^{H_2,H_2^+,H^-}$, we will separate the various contributions using the Balmer line emission

model for $B_{3,4\rightarrow2}^{H_2,H_2^+,H^-}$ highlighted in section appendix A. The steps for this are highlighted in figure 4 (which is step 3 in figure 2) and use the electron density and electron temperature obtained from Stark broadening and the atomic analysis:

3.1) The H_2 contribution of $H\alpha$ and $H\beta$ are estimated using an assumed relation between the H_2 density and the electron temperature, which is obtained from SOLPS simulations (more information is provided below and in section 5.1).
3.2) This H_2 contribution is subtracted from the total $H\alpha$ and $H\beta$ brightnesses attributed to plasma–molecule interactions to obtain the $H\alpha$ and $H\beta$ brightnesses attributed to H_2^+ and H^-.
3.3) The ratio of those $H\alpha$ and $H\beta$ brightnesses are used to separate the $H\alpha$ emission attributed to H_2^+ and H^-.

We have used SOLPS-ITER simulation results from TCV and MAST-U to establish a relation between the expected H_2 density times the pathlength ΔL and the (excitation) electron temperature [32]—$g_{H_2}(T_e^E) \approx \Delta L n_{H_2}$, which is used to estimate the Balmer line brightnesses attributed to H_2—$B_{n\rightarrow2}^{H_2}$ as shown in equation (3). After having estimated $B_{3,4\rightarrow2}^{H_2}$, this is used to estimate the $H\alpha$ and $H\beta$ emission attributed to H_2^+ and H^-: $B_{3,4\rightarrow2}^{H_2^+} + B_{3,4\rightarrow2}^{H^-} = B_{3,4\rightarrow2}^{H_2,H_2^+,H^-} - B_{3,4\rightarrow2}^{H_2}$.

$$B_{n\rightarrow2}^{H_2} = g_{H_2}(T_e^E) n_e PEC_{n\rightarrow2}^{H_2}(n_e, T_e^E). \tag{3}$$

Plasma–molecule interactions involving H_2^+ and H^- lead to different $H\beta/H\alpha$ ratios as shown in figure 5, which is calculated using data from Yacora (on the Web) [22, 23]. This distinction can be used to quantitatively separate emission contributions from H^- and H_2^+ using equation (4), which can be readily obtained when the $B_{3,4\rightarrow2}^{H_2^+,H^-}$ brightnesses are expressed using a plasma-slab model (equation (A2)). We use the Stark broadening derived electron density n_e and the electron impact excitation emission derived temperature (T_e^E) to interrogate the required PECs as this is a more reliable overall temperature (with uncertainty) indicator of the plasma—especially for a hotter plasma [10]—which ultimately is important for MAI estimates (section 2.5.2). However, using the EIR derived temperature instead for any of the molecular estimates would not change any of the obtained conclusions in the tested conditions, apart from reducing MAI rates.

$$f_{H_2^+,mol.H\alpha} \equiv \frac{B_{3\rightarrow2}^{H_2^+}}{B_{3\rightarrow2}^{H_2^+} + B_{3\rightarrow2}^{H^-}} = \frac{1}{1+C}$$

$$C = \frac{PEC_{3\rightarrow2}^{H^-}(n_e, T_e^E)\left[PEC_{3\rightarrow2}^{H_2^+}(n_e, T_e^E)\,(H\beta/H\alpha)|_{H^-,H_2^+} - PEC_{4\rightarrow2}^{H_2^+}(n_e, T_e^E)\right]}{PEC_{4\rightarrow2}^{H^-}(n_e, T_e^E) - PEC_{3\rightarrow2}^{H^-}(n_e, T_e^E)\,(H\beta/H\alpha)|_{H^-,H_2^+}}. \tag{4}$$

Now we have all the information required to determine all the emission contributions to $H\alpha$, which are summarised in equation (5).
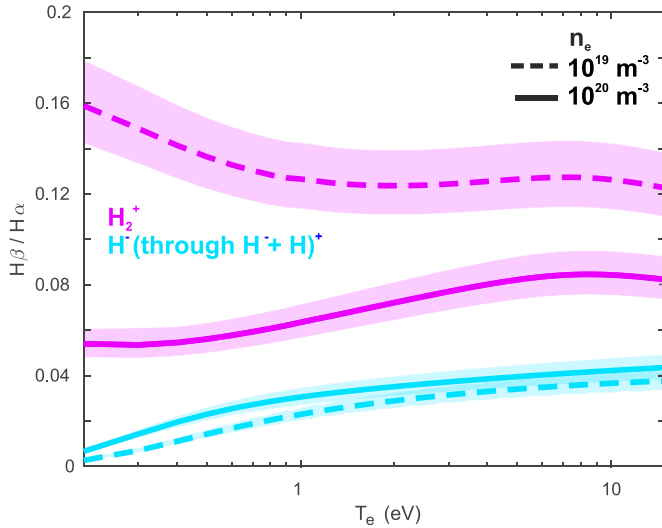
Figure 5. $H\beta/H\alpha$ ratio using YACORA PEC coefficients for H_2^+ and $H^- + H^+$ for two different electron densities as function of T_e with shaded uncertainties (based on the assumed 25% uncertainty for molecular coefficients).

$$B_{3\to2}^{atom,extrapolated} = B_{n\to2}^{exc}\frac{PEC_{3\to2}^{exc}(n_e,T_e^E)}{PEC_{n\to2}^{exc}(n_e,T_e^E)} + B_{n\to2}^{rec}\frac{PEC_{3\to2}^{rec}(n_e,T_e^R)}{PEC_{n\to2}^{rec}(n_e,T_e^R)}$$

$$B_{3\to2}^{H_2,H_2^+,H^-} = B_{3\to2}^{tot,measured} - B_{3\to2}^{atom,extrapolated}$$

$$B_{3\to2}^{H_2} = g_{H_2}(T_e^E)n_ePEC_{3\to2}^{H_2}(n_e,T_e^E)$$

$$B_{3\to2}^{H_2^+} = (B_{3\to2}^{H_2,H_2^+,H^-} - B_{3\to2}^{H_2}) \times f_{H_2^+,mol.H\alpha}$$

$$B_{3\to2}^{H^-} = (B_{3\to2}^{H_2,H_2^+,H^-} - B_{3\to2}^{H_2}) \times (1 - f_{H_2^+,mol.H\alpha}).$$

$$(5)$$

2.4. Molecular contributions to $n > 4$ Balmer line emission

Up until this point in the analysis, we have not taken into account that the medium-n Balmer lines can also be influenced by plasma–molecule interactions. Although plasma–molecule interactions predominantly impact $H\alpha$ and $H\beta$, the impact on the medium-n Balmer lines may not be fully negligible. We can account for this by enforcing consistency between the molecular contributions to $H\alpha$ & $H\beta$ and the medium-n Balmer lines used in the atomic part of the analysis.

This is achieved by first extrapolating $B_{3\to2}^{H_2,H_2^+,H^-}$ to the medium-n Balmer lines—$B_{n\to2}^{H_2,H_2^+,H^-}$—figure 6, which represents step 4 in figure 2. This extrapolation is achieved by estimating the ratio between the medium-n Balmer lines and $H\alpha$ for H_2, H_2^+, H^- separately and multiplying those ratios with the respective $B_{n\to2}^{H_2}, B_{n\to2}^{H_2^+}, B_{n\to2}^{H^-}$ brightnesses, which are summed to provide $B_{n\to2}^{H_2,H_2^+,H^-}$.

Secondly, using $B_{n\to2}^{H_2,H_2^+,H^-}$ for the medium-n Balmer lines, the atomic contribution of the medium-n Balmer lines is estimated—$B_{n\to2}^{atom}$ (equation (6)). Here, it is assumed that the total measured medium-n Balmer line brightness is its atomic part plus its molecular part—which was used for $H\alpha$ in equation (1).
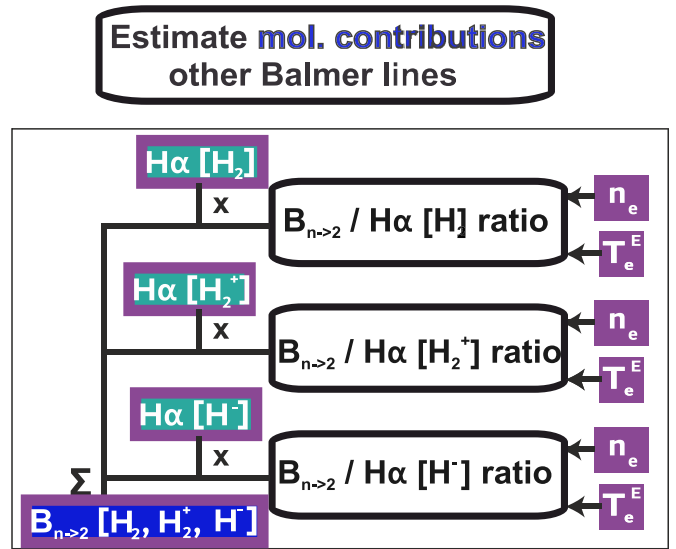

Figure 6. Schematic analysis flow chart for estimating the molecular contributions to the other Balmer lines based on the various $H\alpha$ 'molecular' emission channels. This represents step 4 'Separate mol. contributions other Balmer lines' in figure 2.

With those updated $B_{n\to2}^{atom}$ estimates for the medium-n Balmer lines, the entire analysis is re-executed, yielding modified values for all estimates—including a new extrapolated $B_{n\to2}^{H_2,H_2^+,H^-}$ for the medium-n Balmer lines. This is repeated iteratively (see appendix 2.1) until these extrapolated brightnesses reach a converged value which has a fully self-consistent solution between $B_{3\to2}^{H_2,H_2^+,H^-}$ and $B_{n\to2}^{H_2,H_2^+,H^-}$.

$$B_{n\to2}^{tot,measured} = B_{n\to2}^{H_2,H_2^+,H^-} + B_{n\to2}^{atom}$$

$$B_{n\to2}^{atom} = B_{n\to2}^{tot,measured} - B_{n\to2}^{H_2} - B_{n\to2}^{H_2^+} - B_{n\to2}^{H^-+H^+}$$

$$B_{n\to2}^{atom} = B_{n\to2}^{tot,measured} - B_{3\to2}^{H_2}\frac{PEC_{n\to2}^{H_2}(n_e,T_e^E)}{PEC_{3\to2}^{H_2}(n_e,T_e^E)}$$

$$- B_{3\to2}^{H_2^+}\frac{PEC_{n\to2}^{H_2^+}(n_e,T_e^E)}{PEC_{3\to2}^{H_2^+}(n_e,T_e^E)} - B_{3\to2}^{H^-}\frac{PEC_{n\to2}^{H^-+H^+}(n_e,T_e^E)}{PEC_{3\to2}^{H^-+H^+}(n_e,T_e^E)}.$$

$$(6)$$

When we compare results with and without this iterative approach (section 5.3) we find that the $B_{3\to2}^{H_2,H_2^+,H^-}$ estimate is insensitive to this iteration considering its uncertainties. The iterative approach, however, is important for obtaining accurate estimates of the excitation emission component of the medium-n Balmer lines, which are important for ionisation estimates.

2.5. Inferring radiative losses and MAI/MAR from plasma–molecule interactions

The separated brightnesses of $H\alpha$ are used to determine the various atomic reaction rates/power losses (as is done in [10]), as well as the various MAR/MAI ion sinks/sources and hydrogenic radiative power losses (table 1) related to excited
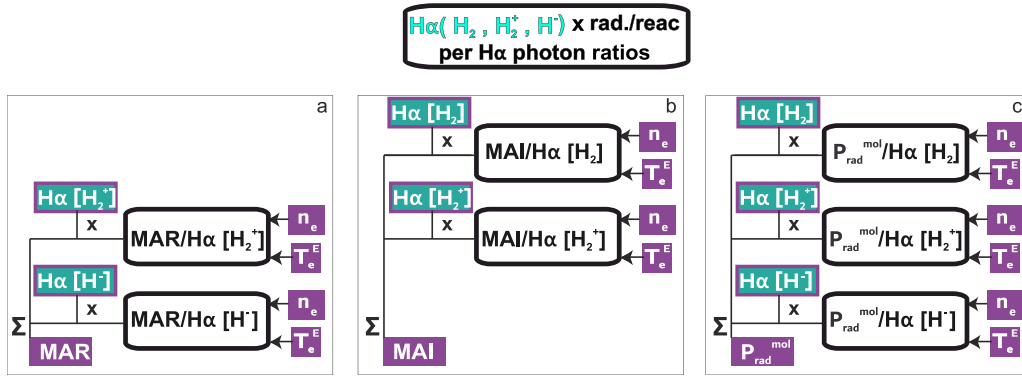
Figure 7. Schematic analysis flow chart for estimating MAR (a), MAI (b) and radiative loss rates (c) from the separated $H\alpha$ 'molecular' emission pathways. This represents step 5 '$H\alpha(H_2, H_2^+, H^-)$ x rad./reac per $H\alpha$ photon ratios' in figure 2.

atoms after plasma–molecule interaction. The analysis steps of this approach are shown schematically in figure 7, which is step 5 in figure 2. For all the cases in figure 7, the separated $H\alpha$ brightnesses are multiplied with the 'effective radiative loss (figure 7(c)) (or MAI/MAR reaction rate—figures 7(a) and (b) per emitted $H\alpha$ photon' using the Stark broadening inferred n_e and electron-impact excitation derived T_e^E. This provides radiative losses (or MAI/MAR reaction rates) for each process, which are summed to provide the total hydrogenic radiative power loss estimates and MAR/MAI rates.

2.5.1. Inferring hydrogenic line radiative losses from plasma–molecule interactions.

Although $H\alpha$ emission does not lead to significant radiative losses directly, considering most plasma radiation is in the VUV [33], it can be an indicator for significant radiative losses. $H\alpha$ emission, corresponding to the $3 \to 2$ transition, directly implies also the presence of $Ly\beta$ ($3 \to 1$) emission. Utilising the associated Einstein coefficients and photon energies, 6.5 times more radiative loss arises due to $Ly\beta$ than $H\alpha$ (e.g. $\frac{E_{Ly\beta} \times A_{31}/A_{32}}{E_{H\alpha}} \approx 6.5$). Since $H\alpha$ indicates a transition to the $n = 2$ excited state, the enhancement of $H\alpha$ should also lead to some enhancement of the $n = 2$ excited state, which subsequently results in $Ly\alpha$ emission—which carries 5.8 times more energy than a $H\alpha$ photon.

It is thus clear that, at a minimum, a power loss of the order of ten more than the power loss of $H\alpha$ itself is associated with related (V)UV emission. Since this only covers the influence of plasma–molecule interactions on the $n = 3$ populated state, this is a conservative estimate of the radiative losses due to plasma–molecule interactions. For example, plasma–molecule interactions could potentially directly lead to an enhancement of the $n = 2$ populated state, and thus directly enhance $Ly\alpha$ radiation losses.

It is important to repeat that the power loss estimated here is *radiation from hydrogenic (atomic) emission lines* arising from *excited atoms* after *plasma–molecule interactions. This is different* from radiative losses associated with molecular band emission which has been the subject of previous research [17, 33], where the brightness of several molecular (Fulcher, Werner (VUV)) bands were measured and its associated radiative power loss was estimated to be negligible. Therefore,

the atomic radiative losses from plasma–molecule interactions likely plays a dominant role in the radiative losses attributed to plasma–molecule interactions in detached plasmas.

To estimate radiative power losses due to plasma–molecule interactions, we utilise Yacora (on the Web) [22, 23] to model the most dominant lines ($n < 7$) of the atomic Balmer and Lyman spectra associated with plasma–molecule interactions. These are multiplied with their respective photon energies and summed to estimate the radiated hydrogenic (atomic) power loss due to excited atoms after plasma–molecule interaction. This power is then divided by the $H\alpha$ emission attributed to those channels, obtaining a ratio representing 'total radiated energy (eV) per $H\alpha$ photon' for each individual emission channel (equation (7)). We represent this as ($\frac{P_{rad,L}^{H_2,H_2^+,H^-}}{B_{3\to 2}^{H_2,H_2^+,H^-}}$) where $P_{rad,L}^{H_2,H_2^+,H^-}$ is a line-integrated radiation rate in W m^{-2}, which can be determined by multiplying the respective brightness with the respective 'total radiation per $H\alpha$ photon' coefficient:

$$P_{rad,L}^{H_2,H_2^+,H^-} = B_{3\to 2}^{H_2,H_2^+,H^-} \times \frac{P_{rad,L}^{H_2,H_2^+,H^-}}{B_{3\to 2}^{H_2,H_2^+,H^-}}.$$

$$\frac{P_{rad,L}^{H_2}}{B_{3\to 2}^{H_2}} = \sum_{i=2,3,4,5,6}\sum_{j=1,2;i>j} \frac{PEC_{i\to j}^{H_2}(n_e,T_e)}{PEC_{3\to 2}^{H_2}(n_e,T_e)}$$

$$\frac{P_{rad,L}^{H_2^+}}{B_{3\to 2}^{H_2^+}} = \sum_{i=2,3,4,5,6}\sum_{j=1,2;i>j} \frac{PEC_{i\to j}^{H_2^+}(n_e,T_e)}{PEC_{3\to 2}^{H_2^+}(n_e,T_e)}$$

$$\frac{P_{rad,L}^{H^-}}{B_{3\to 2}^{H^-}} = \sum_{i=2,3,4,5}\sum_{j=1,2;i>j} \frac{PEC_{i\to j}^{H^-+H^+}(n_e,T_e)}{PEC_{3\to 2}^{H^-+H^+}(n_e,T_e)}. \quad (7)$$

Examples of these coefficients are shown in figure 8 and are compared to the minimum power loss expected from a $H\alpha$ photon due to molecular reactions (when also accounting for associated $Ly\beta$ and $Ly\alpha$ emission). This indicates roughly 20–100 eV power loss per observed $H\alpha$ photon that is due to H_2^+ and H^- contributions to $H\alpha$. This is (especially for H_2^+) significantly larger than the minimum expected radiative losses based on $H\alpha$, which indicates that H_2 plasma chemistry can also result in $n = 2$ excited atoms, without having to go through the $n = 3$ state.
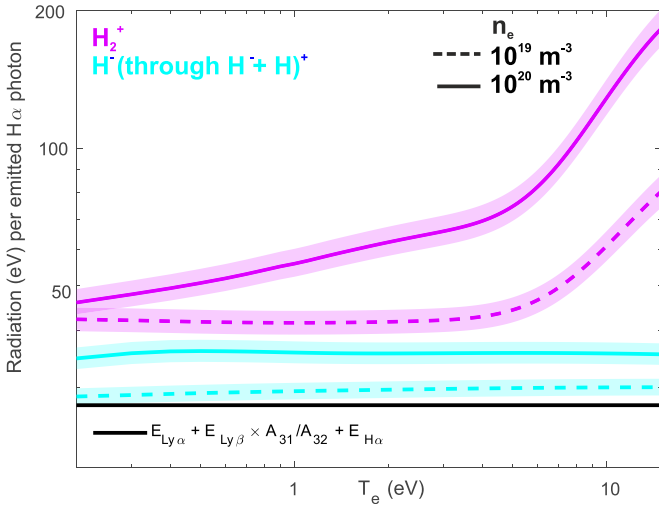
Figure 8. Radiative loss (eV) per emitted $H\alpha$ photon derived from molecular contributions associated with H_2^+ and H^- (assuming excited H atoms arising from plasma–molecule interactions involving H^- comes from the $H^- + H^+$ reaction) at different electron densities. The uncertainty margins arise from the assumed 25 % uncertainty in all PECs attributed to H_2 plasma chemistry. The black curve shows the roughly expected power loss directly explainable by the $H\alpha$ photon (e.g. if one would have the power loss of a $H\alpha$ photon $(3 \to 2)$ plus associated $Ly\alpha$ $(2 \to 1)$ and $Ly\beta$ photons $(3 \to 1)$ per emitted $H\alpha$ photon).

2.5.2. Inferring ion sinks/sources (MAR/MAI) from plasma–molecule interactions. Similarly to how the radiative losses per $H\alpha$ photon are calculated above, one can also calculate ion sinks/sources (MAR/MAI) per $H\alpha$ photon—equation (8) for H_2 and H^-. For the MAR/MAI rates we use AMJUEL [29–31, 34] rates H4 7.2.3a—MAR H^-; H4 2.2.10—MAI H_2.

$$
\begin{aligned}
\left.\frac{MAR}{H_\alpha^{\text{mol}}}\right|_{H^-} &= \frac{MAR_{H^-}(n_e, T_e)}{PEC_{3\to2}^{H^-+H^+}(n_e, T_e)} \\
\left.\frac{MAI}{H_\alpha^{\text{mol}}}\right|_{H_2} &= \frac{MAI_{H_2}(n_e, T_e)}{PEC_{3\to2}^{H_2}(n_e, T_e)}.
\end{aligned} \tag{8}
$$

Calculating MAR/MAI ion sinks/sources for H_2^+ requires additional steps as not only the *destruction* of H_2^+ matters, which can result in excited H atoms thus providing the $B_{n\to2}^{H_2^+}$ we infer, *but also the creation process of H_2^+*. H_2^+ can be created either through molecular charge exchange (CX) $(H_2 + H^+ \to H_2^+ + H)$, *which turns a plasma ion into a neutral*, or ionisation of H_2 $(e^- + H_2 \to 2e^- + H_2^+)$ which *does not turn a plasma ion into a neutral*. When H_2^+ reacts with an electron, there are $3 \times 2 = 6$ possible outcomes: 1,2) $e^- + H_2^+ \to H + H$ (AMJUEL reaction H4 2.2.14) is MAR for molecular CX and MAD for H_2 ionisation; 3,4) $e^- + H_2^+ \to H^+ + H$ (AMJUEL reaction H4 2.2.12) is MAD for molecular CX and MAI for H_2 ionisation; 5,6) $e^- + H_2^+ \to H^+ + H^+$ (AMJUEL reaction H4 2.2.14) is MAI for molecular CX and MAI (x2) for H_2 ionisation.

As neither of those H_2^+ creation processes result in excited atoms, we cannot extract information on which process is dominant using only the Balmer line spectra. Instead, we need

to model the relative strength of the two H_2^+ creation process based on n_e and T_e^E using their reaction rates (equation (9)). This assumes the electron density equals the hydrogen ion density and makes assumptions on the distribution of vibrational states (see section 5.5). For $<\sigma v>_{e^- + H_2 \to 2e^- + H_2^+}$ we use data from [18] (for deuterium), whereas from $<\sigma v>_{H^+ + H_2 \to H + H_2^+}$ we use data from AMJUEL H4 2.2.9.

$$
f_{H_2^+ fromCX} = \frac{<\sigma v>_{H^+ + H_2 \to H + H_2^+}}{<\sigma v>_{H^+ + H_2 \to H + H_2^+} + <\sigma v>_{e^- + H_2 \to 2e^- + H_2^+}}. \tag{9}
$$

We use this model and combine it with the possible MAI/MAR outcomes to calculate the MAI/MAR to H_α emission ratios for H_2^+ shown in equation (10). The notation MAR/MAI/MAD for the rates of equation (10) refers to what the process would be if H_2^+ is purely created through molecular CX (e.g. $f_{H_2^+ \text{ from } CX} = 1$). The impact of different reaction rates on $f_{H_2^+ \text{ from } CX}$ and subsequently the 'MAR and MAI to H_α emission coefficient ratios' are discussed in section 5.5.

$$
\begin{aligned}
\left.\frac{MAR}{H_\alpha^{\text{mol}}}\right|_{H_2^+} &= \frac{f_{H_2^+ fromCX}(n_e, T_e) MAR(n_e, T_e)}{PEC_{3\to2}^{H_2^+}(n_e, T_e)} \\
\left.\frac{MAI}{H_\alpha^{\text{mol}}}\right|_{H_2^+} &= \frac{(2 - f_{H_2^+ fromCX}(n_e, T_e)) MAI(n_e, T_e)}{PEC_{3\to2}^{H_2^+}(n_e, T_e)} + \cdots \\
&\quad \frac{(1 - f_{H_2^+ fromCX}(n_e, T_e)) MAD(n_e, T_e)}{PEC_{3\to2}^{H_2^+}(n_e, T_e)}.
\end{aligned} \tag{10}
$$

Figure 9, which shows the calculated MAR/MAI per $H\alpha$ photon, indicates that at detachment relevant temperatures $(T_e < 3$ eV) H_2^+ and H^- have (within experimental uncertainty) similar MAR per $H\alpha$ photon ratios (4–7). MAI starts to dominate over MAR for H_2^+ at $T_e > 3$ eV. The MAI per $H\alpha$ ratio is particularly sensitive to T_e for $T_e > 3$ eV due to the dependence of $f_{H_2^+ \text{ from } CX}$ on T_e. Considering that the inferred T_e will have an uncertainty, this likely leads to large uncertainties in the MAI estimations.

3. Verification using synthetic diagnostic techniques

There are numerous ways in which the analysis approach uses a simplified emission model, which may not accurately reflect reality. For instance, the analysis approach simplifies the emission along the line of sight as a dual slab model (appendix A and section 2.1) with the same electron density and two different electron temperatures. In reality the plasma profiles along the line of sight vary and the various emission processes can occur at different positions along the line of sight [10, 35]. Additionally, the analysis assumes $Z_{\text{eff}} = 1$, which is not necessarily true. Those limitations are not necessarily problematic as the aim of the analysis is not to retrieve the emission profile along the line of sight but to extract the various line-integrated ion sources/sinks and power losses in the divertor.

The performance of the analysis to extract ion sources/sinks and power losses must be tested. One way of doing this is
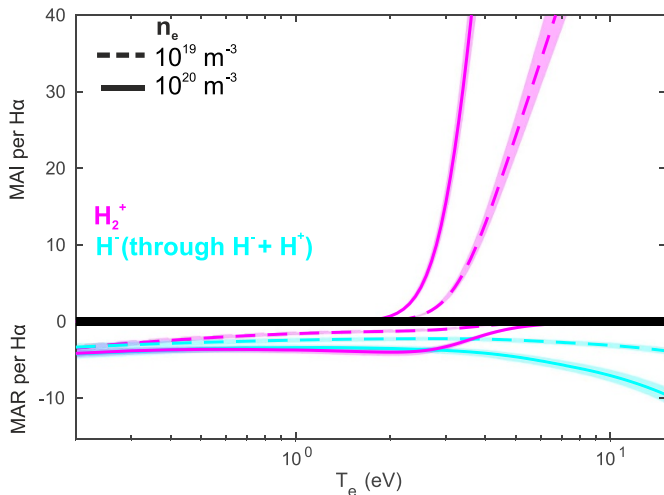
Figure 9. MAR (negative) and MAI (positive) per emitted $H\alpha$ photon for H_2^+, H^- at different electron densities. The black curve represents zero. The uncertainties are provided by the default assumption of an uncertainty of 25 % on all used molecular reaction rates and emission coefficient in addition to an assumed H_2 temperature range ([0.37–10] eV using a log-uniform distribution)—see section 5.5. The indicated uncertainties are 68% confidence margins.

to verify its outcomes against a 'known' case, which can be achieved by using plasma-edge simulations to simulate the spectra a spectrometer would see synthetically. This can then be analysed in the same way as experimental data and those outputs can be compared 'directly' outputs from the simulations.

In this work we apply this synthetic testing approach to SOLPS-ITER simulations of TCV and MAST-U plasmas. This involves both a D_2 gas puff scan (TCV, MAST-U) and a N_2 gas puff scan (MAST-U). The methods used for this have been developed in [10, 25] and account accurately for the various spectrometer uncertainties.

To simulate the Balmer line brightnesses attributed to H_2 chemistry involving H_2, H_2^+, H^-, H_3^+, Yacora (on the Web) collisional radiative modelling results [23, 22] are used in conjunction with the simulated electron temperature, electron density, molecule (H_2) density as well as the ion (H^+) temperature. The temperature of H^- is assumed to be equal to the H_2 temperature plus a random number between 0 and 2.2 eV as H^- arises from reactions between the plasma and H_2 and a part of the Franck–Cordon energy binding H_2 is released to H^-. ADAS is used for the electron excitation impact (of H) and EIR (of H^+) Balmer line emission contributions [26, 27].

The densities for H_2^+, H^-, H_3^+ must be known to accurately model the Balmer line emission from excited hydrogen atoms after those ions react. Such species are, by default, not ('fully') treated in SOLPS-ITER. Generally, only H_2^+ is included. However, it is designated as a 'test specie' in Eirene where it remains static (e.g. there is no transport) after being created. Additionally, there is some discussion on the isotope dependency of the rates leading to and/or breaking up H_2^+, H^- [36]; which is further discussed in section 5.5.

We overcome the above limitations of the information from SOLPS-ITER corresponding to H_2^+, H_3^+, H^- to H_2 by using a balance (which neglects transport) between the creation and destruction rates of these species from H_2 to 'post-process' the H_2^+, H_3^+, H^- densities after obtaining the SOLPS-ITER results [10]. For the H_2^+ rates we employ the same rates as discussed in section 2.5.2 (using the reported H_2 temperatures from the simulation). It is important to warn the reader that these ratios are still being debated in literature and may have large uncertainties, see section 5.5. Therefore, significant deviations can occur between the post-processed results, the direct SOLPS-ITER outputs and the experimental results when it comes to the H_2^+ (and H^-, H_3^+) densities.

Although the goal of this analysis is to retrieve line-integrated parameters from line-integrated spectroscopy, it would be beneficial to have estimates of the various parameters also along the lines-of-sight. Given the complexities of modelling the various molecular densities along the line of sight, this could be achieved by applying the shown techniques to 2D filtered camera images of the Balmer line emission in the divertor (see section 5.6).

3.1. Description of results from modeling the Balmer line emission on the SOLPS grid

Now that we have explained how we model the Balmer line emission on the SOLPS grid, we will later use this to perform synthetic testing on the analysis using simulations from both TCV as well as MAST-U. First, however, we show in figures 10(d)–(f) three example emission profiles along a line of sight for both a TCV and MAST-U simulation, together with the respective reaction profiles (figures 10(g)–(i)), electron temperature and electron density profiles (figures 10(j)–(l)). From this we see, indeed, that there is a spatial separation between the various emission profiles in all three cases. Furthermore, in figure 10 we observe that MAI and MAR from H_2^+ occur at different locations spatially. *We can thus conclude that the actual emission and reaction profiles along the line of sight are far more complicated in the test case than is assumed in the analysis chain.*

Secondly, we discuss how the Balmer line emission associated with H_2 plasma chemistry, under the assumptions/limits described, changes the synthetic brightnesses (compared to only accounting for electron-impact excitation and EIR) and how this compares to experimental observations. The simulations used [37] have been compared previously against the accompanying experiment in [5] from a view point of atomic interactions. This provides us with *qualitative* arguments as to how representative the analysed synthetic diagnostic results are of the experiment.

(a) The synthetic diagnostic brightnesses are in quantitative agreement with the experiment if only EIR and electron-impact excitation is considered for the medium-n Balmer lines. The total synthetic $H\alpha$ brightness (related to atomic interactions and H_2 plasma chemistry) is in rough agreement with the total measured $H\alpha$ brightness.
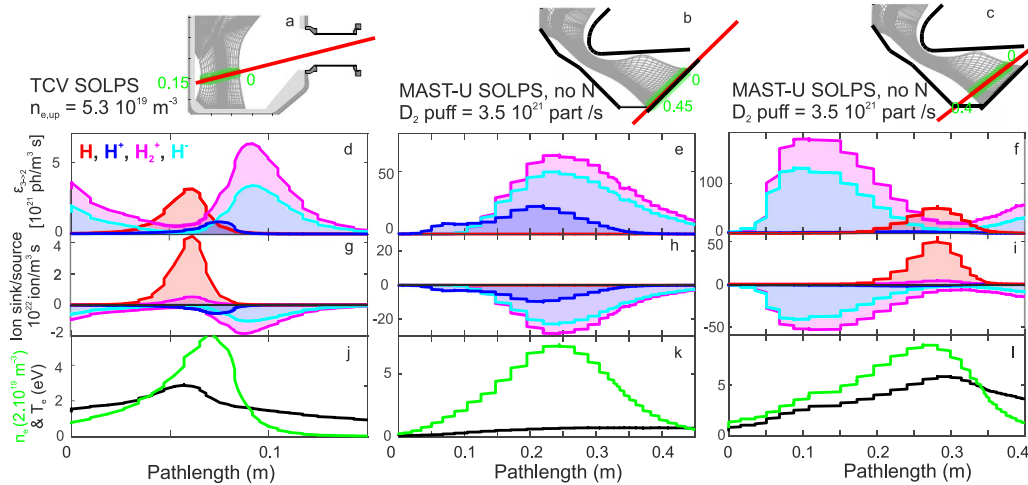
Figure 10. Profiles along an indicated line of sight of the various emission processes, particle source/sink processes as well as the electron temperature and density. This is shown for one TCV case and for two different line of sights for the same MAST-U case. The used line of sights, as well as the divertor geometry and the region where the lines of sight intersect the SOLPS grids are shown.

(b) However, the simulated results indicate a significant fraction of the $n = 5$ Balmer line emission is due to plasma–molecule interactions (mostly due to H_2^+). This lowers the simulated $n = 6/n = 5$ Balmer line ratio from its atomic estimate (~ 0.5) to ~ 0.4 near the target; while the experimental measurement is closer to 0.5 near the target.

As explained in [10], such changes in the Balmer line ratio are expected to have a relatively strong influence on the inferred excitation Balmer line emission. The larger the modification of the medium-n Balmer line ratio by H_2 plasma-chemistry related processes, the more complex and uncertain it is to fully disentangle the 'atomic only' line ratio required for estimating accurately the excitation emission contribution.

Therefore, the application of the analysis is more complex (and has higher uncertainties) in the synthetic diagnostic case than in the experiment.

3.2. Synthetic testing on TCV SOLPS simulations

Now that we have discussed some of the results from simulating the Balmer line emission associated with H_2 plasma chemistry as well as plasma–atom interactions, we show the synthetic testing results using SOLPS simulations for TCV. Figure 11 shows a comparison between various processes obtained 'Direct'(ly) from simulations of a TCV density scan and the same quantities evaluated ('Analysis') through synthetic measurements. Each column of plots corresponds to different sets of constraints that are applied. The technicalities of these constraints are described in more detail in appendix C. For all the cases, an upper electron temperature limit constraint of 20 eV is applied, which is characteristic for these TCV simulations.

Figures 11(a) and (b) shows that the synthetically inferred MAR/EIR ion sinks as well as the radiative power loss associated with H_2^+ and H^- are in quantitative agreement with the

direct SOLPS output if no constraints are employed. There is, however, a strong difference in the ionisation source as well as the radiation associated with electron-impact excitation after the detachment onset (around an upstream density of 3.5×10^{19} m^{-3}). This difference after the detachment onset is caused by an overestimate of the atomic excitation emission caused by underestimating the (atomic only) line ratio $n = 6/n = 5$ near the end of the discharge (~ 0.45 instead of ~ 0.5). The analysis technique shown can thus be used to obtain adequate estimates on EIR, MAR and power losses arising from plasma–molecule interactions. However, during detachment, the ionisation as well as MAI ion source inferences can become unreliable if no constraints are employed.

The periods of poor inference of ion sources can be improved by including additional constraints. As explained in [10], the overestimation of excitation emission is a known complication in cases where the excitation emission is relatively small. Since an overestimation of the excitation emission manifests in an overestimation of the excitation temperature, one can improve the analysis by enforcing temperature constraints [10]. We include two temperature constraints: (a) a constraint at the 'target' (lines of sight near the target) on the electron-impact excitation emission derived target temperature (T_e^E) based on other target temperature estimates (for the synthetic case a ± 1 eV (68% confidence interval) uncertainty is assumed); (b) a temperature constraint based on the observation of the CIII emission front: *below* that front $T_e^E > 8$ eV is given a lower probability while *above* that front $T_e^E < 4$ eV is given a lower probability.

Adding only the target temperature constraint ((c) and (d) of figure 11) leads to a strong improvement of the quantitative agreement of the inferred/directly obtained excitation estimates until even in the detached phase. This can be further improved by adding additional constraints based on the CIII front location. For the synthetic test in figures 11(e) and (f), the impact of the CIII front constraints is marginal ($\sim 5\%$ change in maximum likelihood estimates). However, for other
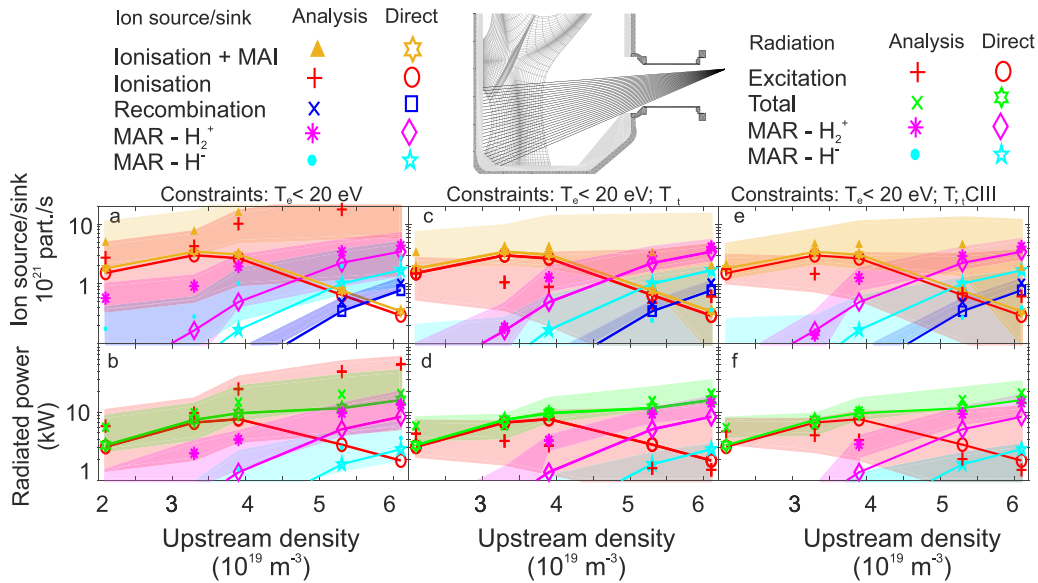
Figure 11. Comparisons between 'Direct' output of SOLPS-ITER modelling of TCV density scan to detachment and the same quantities derived ('Analysis'—with uncertainty margins) from synthetic diagnostic measurements of the same SOLPS-ITER cases: (a) inferred particle balance, including atomic ionisation, electron-ion recombination recombination, MAR from H_2^+ and H^-. (b) Inferred radiative loss channels from atomic (mostly line) emission, including atomic excitation, radiation due to excited atoms from reactions involving H_2^+ and H^- c/d) Power and particle balance comparison between 'Direct' outputs and outputs from the 'Analysis' with the added constraint of target temperature. e/f) Power and particle balance comparison between 'Direct' outputs and outputs from 'Analysis' with an added constraint based on the CIII emission front as well as the target temperature.

cases (such as the experimental case shown in section 4) the impact of the CIII front location constraint can be of a similar magnitude than the impact of the target temperature constraint. These additional constraints also reduce the level of uncertainty in the various estimates. The uncertainties would likely improve further with more detailed profile (e.g. along the divertor leg) temperature estimate constraints.

Even with constraints, the MAI estimates have a significant uncertainty during detachment. This is related to the strong T_e dependence of the MAI/$H\alpha$ ratio (figure 9), which is related to the change-over from H_2^+ being created from molecular CX to it being created from H_2 ionisation (see section 2.5.2). This implies that the MAI estimates are sensitive to inaccuracies in the T_e estimate, which also implies that they are relatively more sensitive to chordal integration effects. The uncertainties in MAI and atomic ionisation are however anti-correlated, and the total uncertainty is reduced when MAI and atomic ionisation is summed (as is done in figure 11).

In the remainder of this work, both temperature constraints from the estimated target temperature as well as the CIII front location are employed for the ionisation and (atomic) radiation estimates when the full analysis (figure 2) is applied, unless stated otherwise.

We observe the electron density is *different* for the EIR, electron-impact excitation, H_2^+ and H^- emission regions (figures 10(d), (g) and (j)). As the analysis assumes the same electron density for all interaction regions based on Stark broadening n_e estimates of the $n = 7$ Balmer line (which is mostly dominated by EIR and is obtained from the synthetic spectrometer in this case), the analysis will overestimate the characteristic electron density for the plasma–molecule

interaction processes. Despite this overestimate, when T_e constraints are employed, the inferred parameters (given their uncertainties) agree with those obtained directly from the simulation.

3.3. Further synthetic testing through 'code experiments' on TCV SOLPS simulations

We can perform further synthetic testing on the simulations shown in the previous section through 'code experiments' by removing certain emission channels from the input of the synthetic brightnesses, after which the full analysis is used to analyse the 'modified' synthetic brightnesses. This is an important part of testing the robustness of the analysis scheme as it enables us to see how well the analysis copes with excluding processes which are not present. This is investigated by:

(a) Removing all molecular emission channels (figures 12(a) and (b)).
(b) Removing the H_2^+ emission channel (figures 12(c) and (d)).
(c) Removing the H^- emission channel (figures 12(e) and (f)).

These cases are shown in figure 12, together with a copy of the analysis in which all emission channels are included, previously shown in figure 11(e) and (f).

Figure 12 generally shows a quantitative agreement between the various particle sinks/sources and power sinks estimated from the analysis and those obtained directly from the code, when one considers the uncertainty of the analysis estimates (68% confidence levels are shown). One exception
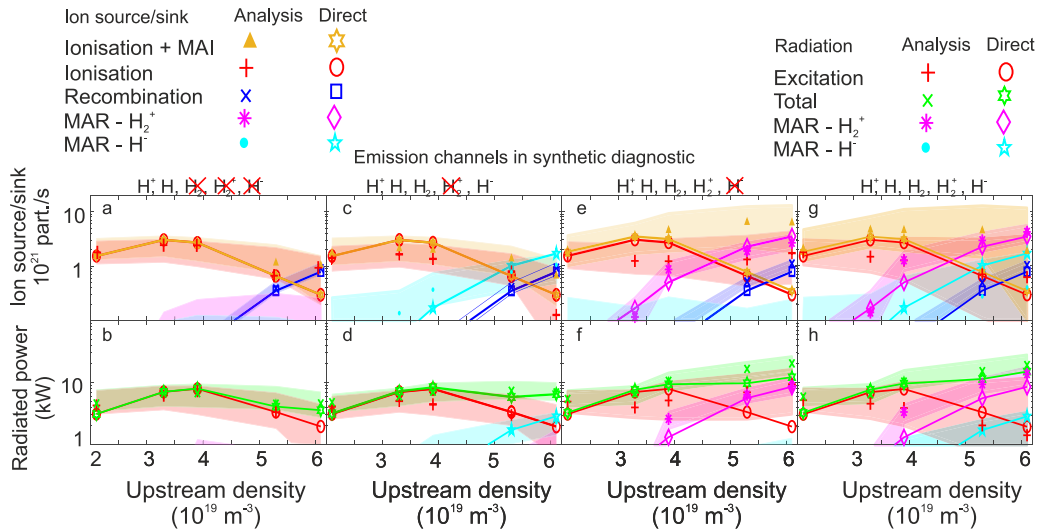
Figure 12. Power and particle balance, similar to figure 11, where certain emission channels have been disabled in the synthetic diagnostic to investigate its influence on the analysis outputs.

to this is the MAI estimate in figures 12(e) and (f) where H^- was not accounted for. This is related with the large uncertainties of MAI discussed previously. We observe that the upper uncertainty level of MAR from H_2^+ and/or H^- are negligible (although not zero) when they have been omitted in the synthetic diagnostic brightness during detachment. This test shows the analysis can correctly point out the lack/presence of MAR and separate MAR from H_2^+ and H^-—as long as their impacts are 'significant'.

We also observe in figure 12 that the quality of the excitation-dependent inferences as well as MAI deteriorates as more emission channels are present in the input synthetic brightnesses. As the contribution of molecules to the $n = 5, 6$ Balmer line increases, the quality of the excitation inferences decreases. This illustrates the necessity of including the various temperature constraints introduced in the previous section.

3.4. Synthetic testing on MAST-U SOLPS simulations

We have applied the similar synthetic testing procedure shown throughout this section to MAST-U SOLPS simulations [38] of a core density ramp as shown in figures 13(a) and (b). In addition, we have applied our synthetic testing procedure to a N_2 seeded scan (with intrinsic carbon impurities) (figures 13(c) and (d)) to have more capabilities of testing our analysis as the plasma fields are different between the fuelling and seeding scans [38]. In this case, we have not used the temperature exclusion constraint based on the CIII front introduced previously as, given the magnetic geometry of the MAST-U Super-X divertor, the CIII front cannot be comfortably tracked using line integrated spectroscopy and instead requires camera diagnostics, such as [39, 40].

We observe that, generally, there is an agreement within uncertainty (68% confidence intervals are shown) between the parameters inferred from the synthetic diagnostic and those obtained directly. The strongest exception to this are excitation related estimates (e.g. ionisation + MAI—orange,

ionisation—red and excitation radiation—red (which is also a part of the total radiation—green)) at the highest N puff rates ($\geq 4 \times 10^{21}$ part s^{-1}), which are significantly overestimated. These overestimates occur because the excitation-related estimates drop below the levels which can be comfortably detected. Those 'detection threshold' levels are higher for the nitrogen seeded case than the core density ramp case because EIR is fully negligible in these cases. This also explains the large uncertainty of the ionisation estimates shown.

In general we see an improved quantitative agreement (especially for MAI) for the MAST-U synthetic testing than the TCV synthetic testing. This is likely attributed to the closed divertor/higher electron densities in MAST-U, resulting in shorter mean free paths. Shorter neutral mean free paths would result in a more strongly localised ionisation region as the neutrals cannot penetrate through the entire divertor leg (as is the case on TCV [5]). As three-body EIR takes over radiative EIR [9, 20] at higher electron densities, the total EIR rate becomes a stronger function of electron density at higher electron densities, resulting in a more localised and stronger EIR region near the target at MAST-U (considering the density is increasing from the x-point towards the target). Both these results lead to a stronger spatial separation between the ionizing and recombining regions along the divertor leg.

3.5. Summary of synthetic testing

The analysis chain has been tested synthetically using both TCV and MAST-U SOLPS simulations in both seeded and non-seeded conditions in combination with synthetic spectroscopy diagnostics to simulate what a spectrometer would observe, which is then analysed in an identical way as the experiment. The emission and reaction profiles along the lines of sight in the analysis are significantly more complicated than the simplified dual-slab model assumed in the analysis chain.

Although the various emission processes occur at different positions along the line of sight, the line-integrated estimates
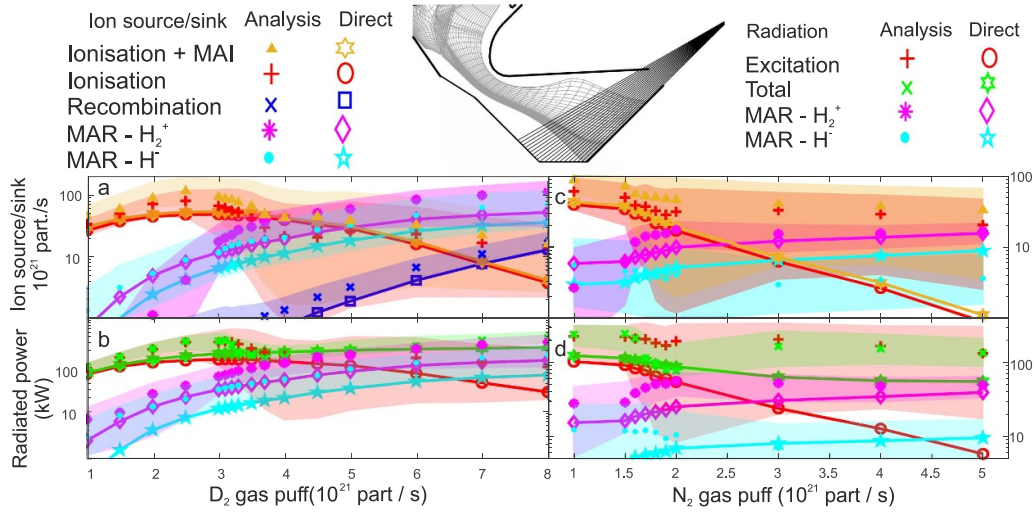
Figure 13. Power and particle balance from estimates from synthetic diagnostic analysis and directly obtained from SOLPS MAST-U simulations [38], similar to figure 11. The results of both a density ramp (with intrinsic carbon impurities) and that of a fixed D_2 puff $(2 \times 10^{21} \text{ part s}^{-1})$ with a N seeding ramp (with intrinsic carbon impurities) are shown.

obtained by the analysis during synthetic testing are generally, considering their uncertainties, in agreement with those obtained by directly integrating the profiles along the line of sight. In addition, we observe that if certain emission processes are removed from the *input* of the analysis, the analysis correctly points out that their contribution is negligible.

This testing suggests the analysis is fairly robust for chordal-integration effects. This is particularly true for the estimates on radiative losses related to excited atoms from H_2 plasma chemistry, MAR and EIR. Ionisation and MAI estimates require additional temperature constraints for higher accuracy.

4. Illustration of the analysis using experimental data from TCV

Although the performance of an analysis can be analysed in detail through synthetic testing, it is beneficial to test an analysis using experimental data. This is particularly true for the analysis used here as there are many uncertainties in simulating the H_2^+ and H^- densities required for simulating the Balmer line emissivities associated with H_2 plasma chemistry in SOLPS-ITER simulations, as discussed in section 3.

We illustrate an example of the *self-consistent* results of the full BaSPMI analysis to separate the hydrogen line brightnesses into its various atomic (excitation/recombination) and molecular (H_2, H_2^+, H^-) contributions. For this we use a conventional divertor L-mode reversed field (unfavourable for H-mode) density ramp discharge with a plasma current of 340 kA. The divertor physics of this discharge has been discussed previously in [5, 24]. The emission spectra is diagnosed using the TCV divertor spectroscopy system (DSS) diagnostic [9, 10]. The divertor geometry with the lines of sight coverage for this diagnostic can be seen in figure 14, adapted from [5, 10]. Diagnostic repeat discharges are used in order to obtain

sufficient diagnostic coverage. The reproducibility of this has been demonstrated in [5]. Three different temperature constraints (for T_e^E) have been employed: (1) the upper temperature limit is 25 eV; (2) temperature constraint based on the CIII 465 nm emission line front which is measured throughout the discharge using line-of-sight spectroscopy (see details in appendix C); (3) a target temperature constraint based on the estimated target temperature by power balance (T_t^{PB}), which was shown and compared against various target temperature estimates (measured and modelled) in figure 10 of [5] yielding a good agreement between the various temperature estimates.

The results of the emission contributions are shown in figure 14 for one line of sight at two different times as a barchart. This is shown for a single line of sight for both the measured Balmer lines ($H\alpha$, $H\beta$, $H\gamma$, $H\delta$) used in the analysis as well as an extrapolated analysis estimate of the $Ly\alpha$ ($B_{2\rightarrow1}$) line, whose totals and individual contributions has been obtained through 'extrapolating' the experimental data of the molecular contributions of $H\alpha$ and the atomic contributions of the medium-n Balmer line n using equation (11) based on combining equations (6) and (2).

$$B_{2\rightarrow1} = \underbrace{\frac{PEC_{2\rightarrow1}^{H_2}(n_e,T_e^E)}{PEC_{3\rightarrow2}^{H_2}(n_e,T_e^E)} \times B_{3\rightarrow2}^{H_2}}_{B_{2\rightarrow1}^{H_2}} + \underbrace{\frac{PEC_{2\rightarrow1}^{H_2^+}(n_e,T_e^E)}{PEC_{3\rightarrow2}^{H_2^+}(n_e,T_e^E)} \times B_{3\rightarrow2}^{H_2^+}}_{B_{2\rightarrow1}^{H_2^+}}$$

$$+ \underbrace{\frac{PEC_{2\rightarrow1}^{H^-}(n_e,T_e^E)}{PEC_{3\rightarrow2}^{H^-}(n_e,T_e^E)} \times B_{3\rightarrow2}^{H^-}}_{B_{2\rightarrow1}^{H^-}} + \underbrace{\frac{PEC_{2\rightarrow1}^{exc}(n_e,T_e^E)}{PEC_{n\rightarrow2}^{exc}(n_e,T_e^E)} \times B_{n\rightarrow2}^{atom,exc}}_{B_{2\rightarrow1}^{exc}}$$

$$+ \underbrace{\frac{PEC_{2\rightarrow1}^{rec}(n_e,T_e^R)}{PEC_{n\rightarrow2}^{rec}(n_e,T_e^R)} \times B_{n\rightarrow2}^{atom,rec}}_{B_{2\rightarrow1}^{rec}}. \quad (11)$$

The illustration of the technique in figure 14 indicates that depending on the plasma conditions (in this case dictated by the timestep in the discharge):

- Plasma–molecule interactions can contribute considerably to hydrogenic line emission. It can *dominate the $H\alpha$, $H\beta$ emission* and it can have a significant impact on *$Ly\alpha$ emission* as well as *medium-n Balmer line emission ($H\gamma$, $H\delta$)*. This has important implication for hydrogenic radiation losses as well as the interpretation of Balmer line divertor spectroscopy measurements.
- A large range of different emission processes can be significant simultaneously; e.g. both EIR, plasma–molecule interactions from H_2^+ and H^- appear to be significant for $H\beta$ at $t = 1.12$ s. This shows the importance of separating the various emission channels.
- The emission processes can change strongly between each hydrogenic transition. We observe that the sensitivity to plasma–molecule interactions diminishes with increasing n of the hydrogenic transition while the sensitivity to EIR increases [10]. Plasma–molecule interactions involving H^- seem to excite the $n = 3$ populational state (e.g. $H\alpha$ emission) in particular.
- We observe that the uncertainties in the electron impact excitation (of H) (EIE) and the emission contribution from H_2^+ are substantial. A closer inspection shows that these uncertainties are *anti-correlated*: low value estimates of the EIE contributions in the statistical samples correspond to high values of the H_2^+ contributions (and visa versa). The EIE contribution is strongly correlated with the excitation-inferred temperature. This illustrates why the various temperature constraints introduced in C are important: without such constraints it is uncertain to distinguish, given the measured data and its uncertainties, electron impact excitation (of H) and emission from excited atoms after plasma reacts with H_2^+.

5. Discussion

5.1. Estimating the Balmer line emission associated with H_2

In section 2.3 we discussed methods to separate the Balmer line emission attributed to H_2 chemistry in its various components (related to H_2, H_2^+, H^-). We started that procedure with assuming an *a priori* $g_{H_2} \approx \Delta L n_{H_2}$ which is a function of T_e^E. That allows us to estimate the brightness associated with H_2: $B_{n \to 2}^{H_2} = g_{H_2}(T_e^E) n_e PEC_{H_2}(n_e, T_e^E)$. In this section we highlight how we obtain this *a priori* function and we discuss its implications. This shows that the expected $B_{n \to 2}^{H_2}$ is insignificant and can be neglected in most divertor conditions.

We obtain this functional form $g_{H_2}(T_e^E)$ by combining TCV [37] and MAST-U [38] SOLPS-ITER simulations in combination with synthetic spectroscopy diagnostics [10, 25] (see section 3). To obtain an estimate for $g_{H_2} \approx \Delta L n_{H_2}$ (equation (12)) we take the synthetic brightness associated with H_2—$B_{n \to 2}^{H_2}$ (which is obtained by integrating the emissivity associated with H_2 along the line of sight) and divide this
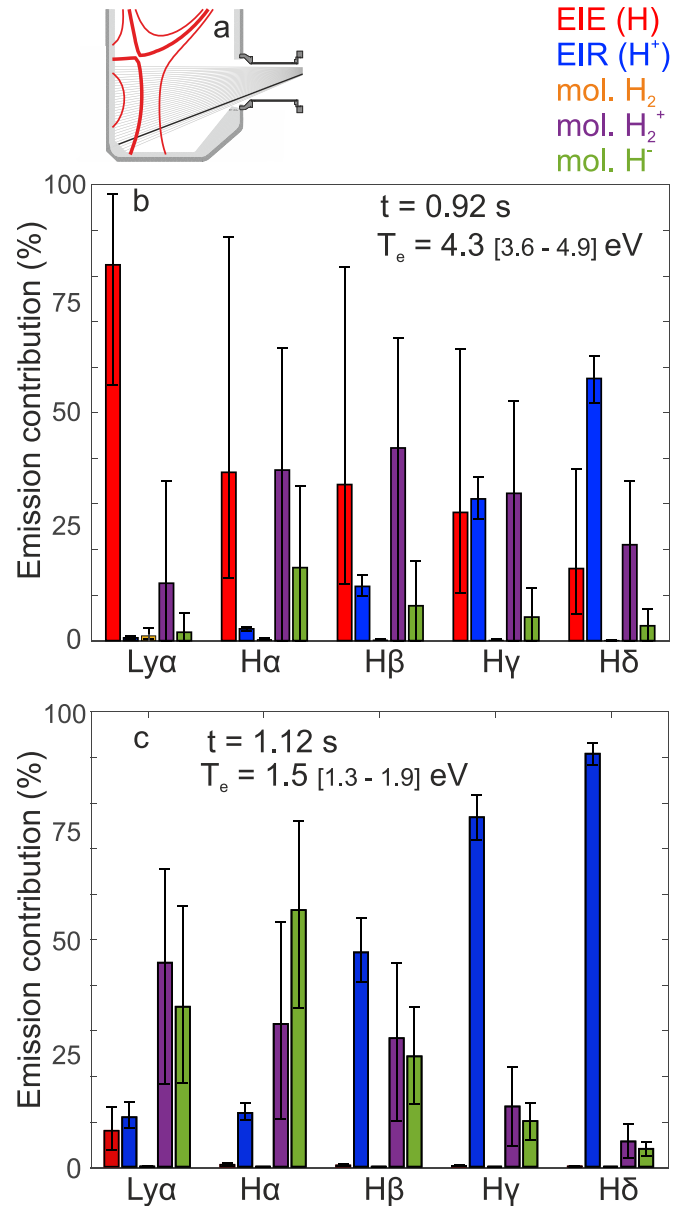
Figure 14. A schematic illustration of the divertor geometry and line of sight is shown (a). A bar-chart of the contributions (%) of various processes is shown (electron-impact excitation 'EIE (H)', electron-ion recombination 'EIR (H^+)', plasma–molecule interaction ('mol.') with H_2, H_2^+ and H^- for various hydrogenic series lines at two different times for a chord close to the target together with indicated estimated electron temperature ranges (b), (c).

by $n_e PEC_{3 \to 2}^{H_2}$ estimated using the electron-impact excitation-emission weighted electron temperature T_e^E and the Stark broadening inferred electron density n_e for that chord using the synthetic diagnostic [10]). We have chosen this formulation because using g_{H_2} with those same electron densities/temperatures in a plasma-slab model would bring us back to—by definition—the synthetically obtained $B_{n \to 2}^{H_2}$.

$$g_{H_2} \equiv \frac{B_{3 \to 2}^{H_2}}{n_e PEC_{3 \to 2}^{H_2}(n_e, T_e^E)} \approx \Delta L \times n_{H_2}. \quad (12)$$

Figure 15. Relation between the excitation Balmer line emission weighted temperature T_e^E and $g_{H_2}(T_e^E) \equiv \frac{B_{3\to2}^{H_2}}{n_e PEC_{3\to2}^{H_2}(n_e, T_e^E)} \approx n_{H_2} \times \Delta L$ (where n_e is the synthetic Stark density). 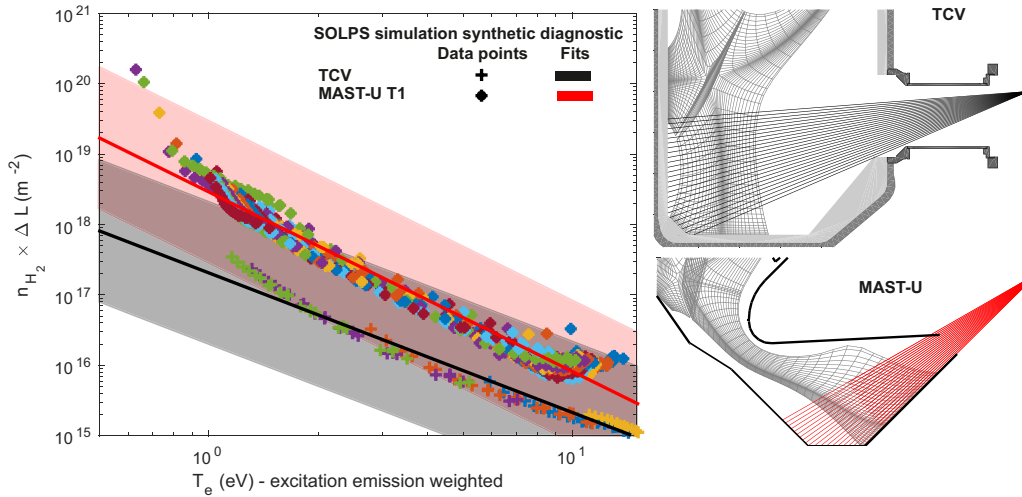Each colour corresponds to a different simulation. Fits through each of the data sets are shown. The TCV data set consists out of 5 simulations [37] (density scan) (26 lines of sight) while the MAST-U data set consists out of 35 simulations [38] (density scan and N_2 seeded) with 20 lines of sight. The corresponding SOLPS grid cells and spectroscopy lines of sight for MAST-U and TCV are also shown.

We then take all the spectroscopy chords in the synthetic diagnostic for all SOLPS simulations and show the obtained g_{H_2} in figure 15 as function of the estimated T_e^E. We find there is a strong relation between g_{H_2} and T_e^E for both TCV and MAST-U simulations. This is a remarkable result as the points in figure 15 all come from different simulations and different chords (thus different plasma positions) of the synthetic diagnostic. In essence, this indicates that having information about the kind of device (e.g. TCV vs MAST-U), the electron excitation temperature and the electron density is sufficient for providing rough estimates on the Balmer line brightness attributed to H_2: $B_{n\to2}^{H_2} = g_{H_2}(T_e^E)n_e PEC_{n\to2}^{H_2}(n_e, T_e^E)$.

We use the g_{H_2} values obtained from the simulations to estimate the relation between g_{H_2} and T_e^E using a fit (linear in log–log space) to which we ascribe an of a factor 100 uncertainty (from a factor 0.1 to 10 log-uniformly distributed) when it is used to estimate $B_{n\to2}^{H_2}$.

The inferred fraction of $H\alpha$ attributed to H_2 (e.g. $B_{3\to2}^{H_2}/B_{3\to2}^{total}$ along the total viewing fan) for the experimental discharge analysed in [24] is shown in figure 16 as function of the 'characteristic' excitation electron temperature (weighted (by $B_{3\to2}^{H_2}$) average T_e^E along the viewing fan). We observe that the *relative* contribution of H_2 to $H\alpha$ is highest at high temperatures. At relatively low temperatures (such as the cases shown in section 4) 4), $\frac{B_{n\to2}^{H_2}}{B_{n\to2}} < 10^{-4}$ (for the result indicated in figure 14). Therefore, even if $g_{H_2}(T_e^E)$ obtained from SOLPS-ITER is strongly underestimated, it would be unlikely that this would influence the obtained solutions.

This result is somewhat in contrast to results from previous studies in limiter devices [41], which have shown that H_2 dissociation may contribute to $H\alpha$ emission. In such conditions, there is a relatively higher molecular density at the location of the hot temperature plasma, whereas in a divertor we obtain high molecular densities at low electron temperatures
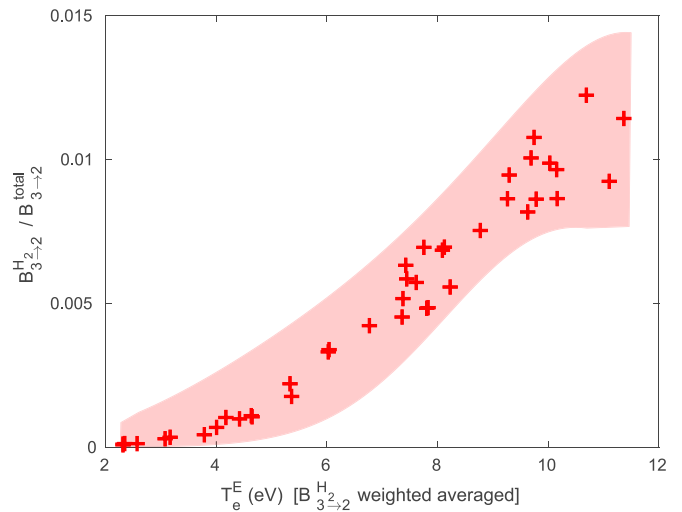
Figure 16. Estimated $H\alpha$ emission fraction attributed to H_2 (summed along the viewing fan) for the experimental discharge analysed in [24] as function of the characteristic T_e^E for that viewing fan (weighted averaged by $B_{3\to2}^{H_2}$).

(see figure 15). Despite this anti-correlation between $n_{H_2}\Delta L$ and T_e, the emission fraction of $H\alpha$ attributed to H_2 increases with T_e (figure 16) because $PEC_{3\to2}^{H_2}(n_e, T_e)$ is strongly correlated with T_e for $T_e < 10$ eV. Furthermore, as was also mentioned in [41], a significant amount of this $H\alpha$ emission in those limiter devices studies could also have arisen from dissociative recombination of H_2^+.

5.2. Additional $H\alpha$ emission contributions not related to plasma–atom interaction and H_2 chemistry

In carbon machines, such as TCV and MAST-U, reactions with hydrocarbons could lead to excited $n = 3, 4$ atoms leading to

additional $H\alpha$, $H\beta$ emission. Additionally, opacity of $Ly\beta$ and $Ly\gamma$ can also lead to additional excited $n = 3, 4$ atoms (and thus $H\alpha$ and $H\beta$ emission). We discuss these two processes here and estimate their importance for TCV.

To obtain an upper limit estimate for the possible atomic emission of hydrocarbons, we assume that *all* neutral carbon from validated SOLPS simulations for TCV [37, 42] exists in the form of hydrocarbons[11]. To map these hypothetical hydrocarbon densities to the $H\alpha$ emission we utilise reaction cross-sections from [43] for CH_4 (the cross-sections for $H\alpha$ emission from [43] are similar for the full range of hydrocarbons presented: $CH_4, C_2H_2, C_2H_6, C_2H_4$). For this extreme case, the estimated $H\alpha$ emission from $n = 3$ excited atoms after hydrocarbon reactions is more than 10^4 smaller than the total $H\alpha$ emission. It is thus unlikely that hydrocarbon chains contribute significantly to the $H\alpha$ emission.

With respect to the effect of opacity, the neutral density along the spectroscopic line of sight remains smaller than $10^{18}\,\mathrm{m}^{-2}$ in SOLPS simulations for TCV [37, 10]. At this level, not much opacity is expected [20, 44], which is indeed confirmed by post-processing the SOLPS simulations using ray-tracing techniques. For the cases shown in figure 14, the impact of photon opacity on $H\alpha$ is estimated to be around 2%. However, opacity can be much more significant on devices with higher neutral densities than TCV. This would impact our analysis as $Ly\beta$ opacity can raise the $H\alpha$ brightness and the analysis would have to be modified to account for this (section 5.6).

5.3. $H\alpha$ as a monitor for MAR and atomic line radiation associated with H_2 plasma chemistry

The increase of $H\alpha$ during detachment, or more specifically the 'anti-correlation between $H\alpha$ and the ion target current' during detachment is observed on several devices [11, 16, 45]. The results derived and described in this paper were applied to a detachment discharge in TCV [24]. This shows the extrapolated $H\alpha$ atomic estimate matches the measured $H\alpha$ until the detachment onset after which the measured $H\alpha$ keeps on increasing while the atomic estimate of $H\alpha$ saturates. We can conclude two things from this result, which is repeated in figure 17(b).

First, we have shown in [24] that the increase of $H\alpha$ during detachment cannot be explained through EIR on TCV, but is explained through plasma–molecule interactions with H_2^+ and H^- (figure 17(b)). Although EIR can be higher on higher divertor density machines, it is likely that the increase of $H\alpha$ in such machines is also, at least partially, due to plasma–molecule interactions with H_2^+ and H^-. In fact, contributions of H_2^+, and/or H^- were also suspected in JET [11] and DIII-D [16] based on the experimentally measured trend and magnitude of $H\alpha$ emission.
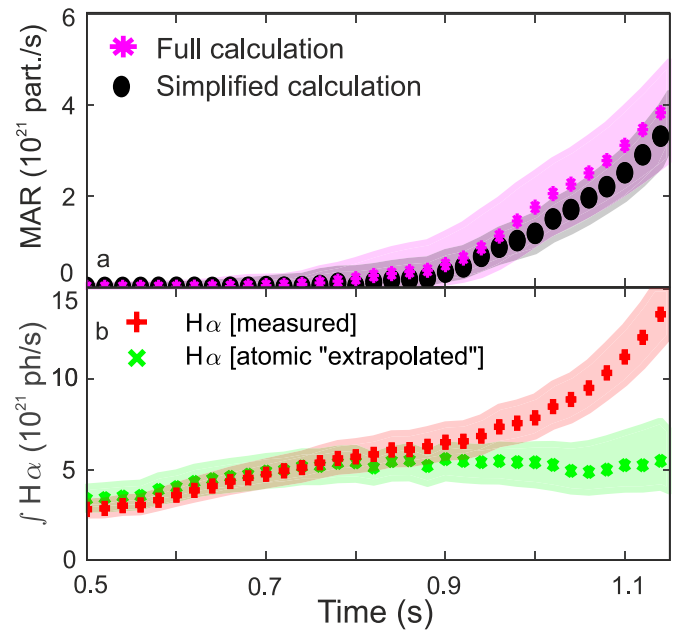
Figure 17. Comparison of analysis techniques based on TCV experimental results for #56 567 which have been discussed, from a divertor physics point of view, in [24] from which the full BaSPMI MAR result and the measured and extrapolated $H\alpha$ have been adopted. (a) Comparison of the 'simplified' divertor MAR calculation (based on multiplying the difference between the atomic extrapolated $H\alpha$ and the measured $H\alpha$ (figure (b) with the 'MAR/$H\alpha$ photon' ratio for H_2^+) against the full BaSPMI result.

Secondly, we have shown in [24] that comparing $H\alpha$ measurements against its atomic extrapolation based on the medium-n Balmer lines is a quick and useful monitor for plasma–molecule interactions involving H_2^+ and/or H^- during detachment, which can be achieved with only the atomic part of the BaSPMI technique. This is also illustrated in figure 17 where we observe that the MAR ion sink starts to appear when there is a bifurcation between the atomic extrapolation of $H\alpha$ and the measured $H\alpha$.

This quick monitor can also be used as a quantitative estimate for radiative power loss and MAR from plasma–molecule interactions, which we denote as a '"simplified" MAR calculation'. This is done by taking the difference between the measured $H\alpha$ and the atomic extrapolation for each plasma chord, which is multiplied with the 'MAR per $H\alpha$ ratio' for H_2^+ (obtained from figure 9), obtained using the inferred n_e, T_e^E from the atomic analysis. The result is a MAR estimate for each chord (e.g. ions per metre squared per second) which is integrated to provide the total MAR sink in the viewing fan (e.g. ions per second). A similar MAR ion sink is obtained if the divertor-integrated $H\alpha$ attributed to plasma–molecule interactions is multiplied with the 'MAR per $H\alpha$ ratio' for H_2^+ using an assumed $n_e = 10^{20}\,\mathrm{m}^{-3}$ and $T_e = 1$ eV.

The above approach only uses the atomic portion of BaSPMI and neglects the impact of H_2 plasma chemistry on the medium-n Balmer lines. Furthermore, this assumes that all Balmer line emission attributed to H_2 plasma chemistry arises from interactions of the plasma with H_2^+. The result of this for

---

[11] Since neutral carbon recombination has been deactivated for most of these simulations ([37]—the SOLPS-ITER default at the time), the sum of the neutral and C^+ densities is utilised as an upper estimate of the neutral carbon density.

the total divertor MAR ion sink is shown in figure 17(a), where it is compared against the full BaSPMI analysis (obtained from [24]). A similar agreement between the simplified and full analysis is obtained for the radiative power loss estimates associated with H_2 plasma chemistry.

These estimates appear to be fairly accurate despite the lack of quantitatively separating $H\alpha$ emission from plasma–molecule interactions with H_2^+ and H^- and despite accounting for the influence of H_2 plasma chemistry on the medium-n Balmer lines. The reason for this is likely that, within experimental uncertainties, the 'MAR per $H\alpha$ ratios' for H_2^+ and H^- are similar (figure 9). This also indicates that, at least for estimating the MAR rate, the calculation is insensitive to chordal integration effects—which is supported with the results from section 3.

However, the full analysis chain would be required to estimate the 'molecular' contributions to the medium-n Balmer line emission, which can be important for ionisation estimates in detached plasmas [24].

Therefore, monitoring $H\alpha$ and comparing it to its atomic estimate is sufficient to:

(a) Show that plasma–atom interactions involving H_2^+ (and possibly H^-) may occur (in environments with low/negligible $Ly\beta$ opacity).
(b) Estimate what their influence on the plasma is in terms of particle and power losses.

Afterwards, one could consider running the full analysis presented to:

(a) Propagate this information to all Balmer lines to get a self-consistent picture which separates each hydrogenic line into its individual contributions, similar to figure 14).
(b) Delineate the plasma-molecule contributions from H_2^+ and H^-.

5.4. Balmer line contributions from plasma–molecule interactions and Fulcher band investigations

Previous research on investigating plasma–molecule interactions in the divertor spectroscopically generally focused on monitoring the molecular band emission, such as the Fulcher band which comes from electronically excited molecules [13, 14, 16] after plasma-molecule *collisions*.

Although plasma-molecule *collisions* are different from plasma-molecule *reactions*, MAR rate estimates from *reactions* with H_2^+ and H^- have been estimated previously using measurements of the Fulcher band. Those measurements provide information on H_2 and its vibrational distribution, which is combined with n_e, T_e estimates and a model or simulations to extrapolate the H_2 density to the H_2^+ density and its resulting MAR rate [13, 14, 16].

This differs from the approach in this work which aims to extract the Balmer line emission arising directly from the excited atoms after plasma–molecule interactions with

H_2^+, H^-. Therefore, it does not require assuming that the location of the H_2 electronic excitation (e.g. Fulcher band emission) is the same as the location of the MAR reactions along the lines of sight. That assumption could be problematic as electronic excitation of H_2 requires fairly high electron temperatures ($T_e > 3$–4 eV), whereas MAR can occur at lower temperatures ($T_e = [1.5 - 4]$ eV). Our measurements in [24] indicate, for instance, that the peak Balmer line emission from excited atoms after *reactions* between the plasma and H_2^+ (and/or H^-) occurs at a different position than the region with the brightest Fulcher band emission [24].

Extrapolating MAR rates out of a Fulcher band analysis requires using a model to predict the creation and destruction rates of H_2^+ and H^-, which may have large uncertainties and isotope dependencies (see section 5.5). The BaSPMI analysis, however, does not[12] rely on such assumptions as it monitors *the destruction of H_2^+ and/or H^- into excited atoms* directly, rather than using rates and models to model the H_2^+ and/or H^- densities based on estimations of the H_2 density.

BaSPMI can be used as an alternative tool to the Fulcher spectra to investigate more closely how such interactions with H_2^+, H^- influence the plasma and provides an indirect tool to investigate the conditions which promote H_2^+, H^- creation. It could for instance be used to study differences in MAR from H_2^+ and/or H^- between carbon and metallic walls (which influences the vibrational state of molecules reflected from the wall, influencing the creation/destruction mechanisms behind H_2^+, H^- [19, 46–48]). As BaSPMI uses Balmer line measurements, it could be a tool which is more straightforward to employ as Balmer line measurements are more routinely employed on tokamaks. They are often easier to diagnose than the Fulcher band, given the high spectral resolution and high sensitivity often required for molecular band studies. Given that BaSMPI uses Balmer line measurements, which can be measured using 2D multi-spectral imaging diagnostics [40], its analysis could in principle be extended to a 2D analysis. For this, however, electron density estimates would be required, which could be obtained using Helium line spectroscopy [49], coherence imaging techniques (for Stark broadening) or Bayesian analysis techniques [50].

BaSPMI is, however, influenced by opacity and requires high quality collisional radiative model results to provide information on how the various H_2 plasma chemistry processes lead to excited hydrogen atoms and resulting atomic line emission [23, 22]. Furthermore, as H_2 ionisation occurs in a similar T_e window as Fulcher band emission, a Fulcher band analysis may provide more accurate MAI (from H_2^+) estimates than BaSPMI.

5.5. Reliance on molecular data: isotope effects and impacts from vibrational states

The Yacora (on the Web) [22, 23] collisional radiative model and AMJUEL database [30] does not (yet) provide explicit

---

12 There is a very weak dependence on such rates for estimating the 'MAR/MAI per $H\alpha$ photon' ratio as this changes depending on whether H_2^+ was created through molecular CX or H_2 ionisation—see section 5.5.
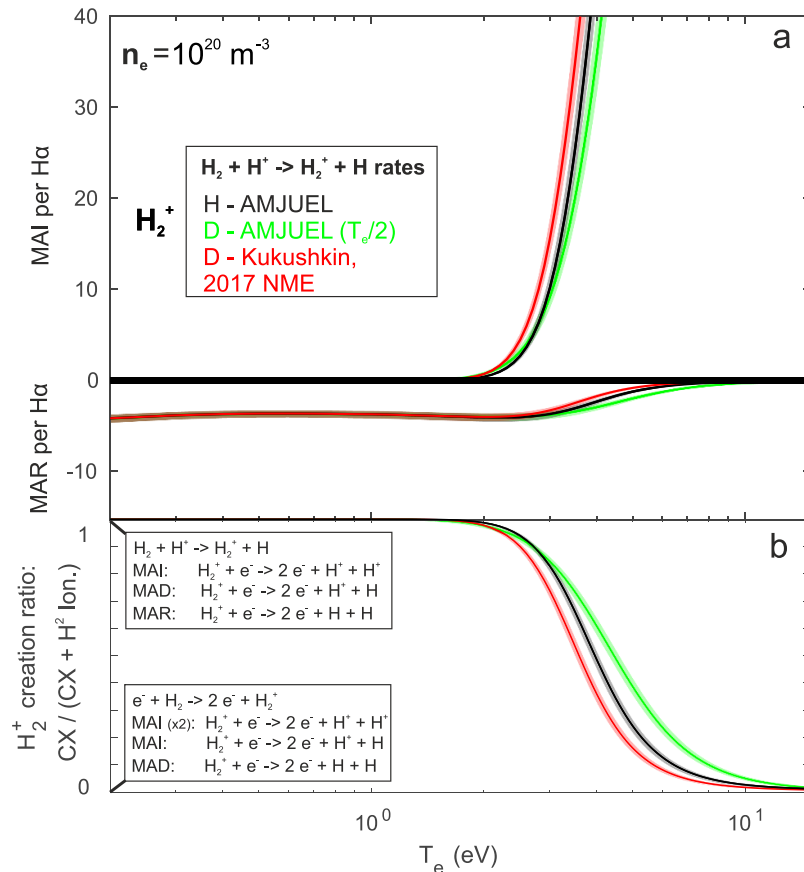
Figure 18. A more detailed version of figure 9. (a) 'MAR/MAI per $H\alpha$' ratios for various molecular charge exchange reaction rates for the creation of H_2^+ as function of T_e. These depend on $f_{H_2^+ \text{ from CX}}$ (e.g. ratio between the CX H_2^+ creation rate and the total H_2^+ creation rate (CX + H_2 ionisation)), which is shown in figure (b), through equation (10).

parallel information for *H* and *D* or *T* related processes. Rather the preponderance of rates for *H* and various assumptions must be made in their application to *D* (and *T*). This is an important caveat of this analysis. If collisional radiative results become available for *D* (and *T*) in the future, they could be used instead in the outlines analysis approach.

In this discussion, it is important to distinguish between two categories of atomic/molecular data. First, there are the actual *creation and destruction rates* of H_2^+ and/or H^-. Those rates are important for modelling the H_2^+ and/or H^- densities based on the H_2 density. Secondly, there are the PECs which provide estimates on the distribution of the excited states of hydrogen atoms *after H_2^+ and/or H^- undergoes a reaction resulting in hydrogen neutrals*. Particularly, some of the rates of the first category are discussed in literature to have potentially strong isotope dependencies [36, 51] as well as significant dependencies on the vibrational distribution of H_2.

Our analysis almost fully depends on only rates from the second category. However, we use rates from the first category for estimating the 'MAR/MAI per $H\alpha$ photon' ratio for H_2^+ (equation (10)) as we must distinguish between H_2^+ creation through molecular CX and H_2 ionisation (equation (9)). Distinguishing between these two different H_2^+ creation mechanisms depends on the H_2^+ molecular CX rate (equation

(9)), which in particular is expected to be both isotope and H_2 vibrational level dependent [36].

From a detailed analysis we, however, find that using different models for the molecular CX rate only has a negligible impact on the 'MAR/MAI per $H\alpha$ photon' ratio, despite the molecular CX rate itself changing by an order of magnitude in detachment-relevant conditions ($T_e = [1-3]$ eV) between the different models used. We perform this analysis by calculating the fraction of H_2^+ created by molecular CX $f_{H_2^+ \text{ from CX}} = \frac{<\sigma v>_{H_2 + H^+ \rightarrow H_2^+ + H}}{<\sigma v>_{H_2 + H^+ \rightarrow H_2^+ + H} + <\sigma v>_{e^- + H_2 \rightarrow 2e^- + H_2^+}}$ equation (9) (figure 18(b)) and its impact on the 'MAI/MAR rate per $H\alpha$ photon ratios' for H_2^+ (equation (10)), shown in figure 18(a). The result for three different molecular CX rates are shown: 1–the default rates from AMJUEL for hydrogen; 2–the default rates from AMJUEL where the rates are shifted by dividing the electron temperature by two to model the deuterium rate[13]; 3–an alternative rate for deuterium investigated in [36]. The vibrational distribution is modelled using an assumed H_2 temperature, which has been varied in the Monte Carlo uncertainty processing throughout the entire validity regime [0.37–10 eV] of the data. We find in figure 18 that the impact of the various rates on the calculated 'MAI/MAR rate

---

[13] This is the default in Eirene [30].

per $H\alpha$ photon ratios' for H_2^+ is small. Therefore, our analysis seems to be robust against these uncertainties.

The reason for this is that our analysis only depends on $f_{H_2^+ \text{ from CX}}$. Modelling the H_2^+/H_2 ratio instead based on a no-transport model, however, would depend on the *relative ratio between the sum of the H_2^+ creation and destruction mechanisms*—e.g. proportional to $<\sigma v>_{H_2+H^+\rightarrow H_2^++H} + <\sigma v>_{e^-+H_2\rightarrow 2e^-+H_2^+}$. The latter ratio would change by an order of magnitude if the molecular CX rate is dominant and changes by an order of magnitude. $f_{H_2^+ \text{ from CX}}$, however would be insensitive to such changes in the molecular CX rate (as long as this rate is significantly larger than the H_2 ionisation rate).

There is not only an expected isotope dependence on the H_2^+ creation rate, but also on the H^- creation rate. Experimental evidence indicates the cross-sections for creating D^- at low vibrational levels are much smaller than for H^- [51]. However, to allow for the largest degree of flexibility, we have opted to allow for the possibility of reactions with H^- resulting in Balmer line emission in our analysis. As our analysis does not depend on the reaction rates for creating H^-, it could potentially provide clarity on the presence of H^-—but that requires further investigation.

The discussion in this section also applies to the application of this analysis for different isotope mixtures such as D&T or H&D. If the impact of such isotope mixtures on the molecular PECs as well as on the MAR/MAI per $H\alpha$ photon ratios is limited ($<50\%$), it should be possible to apply this analysis. Possibly high resolution spectroscopy to separate the H, D, T Balmer lines could help separate reactions per isotope combination in such conditions.

5.6. The applicability of these techniques to different devices and its implications

In this work we have applied an analysis technique to separate the Balmer line emission from its various atomic and molecular channels; after which the power losses due to each individual channel as well as the ion sources and sinks can be estimated. Its workings have been demonstrated analysing synthetic diagnostic results obtained from SOLPS simulations of both TCV and MAST-U. Emission characteristics very likely differ, however, between TCV, MAST-U and higher power and/or density tokamaks such as ASDEX-Upgrade and JET. This raises the question how generally applicable our presented analysis techniques are. Below we address this from the point of view of plasma conditions, viewing geometry and diagnostic capabilities.

5.6.1. Applicability related to plasma conditions. Generally, the applicability of this analysis technique has been discussed in depth in [10] where only atomic processes are considered for the Balmer line emission. It was reasoned that the atomic analysis of the Balmer lines should be generally applicable in both attached and detached conditions. We can make various

quantitative estimates of the roles of plasma–molecule interactions on MAR and radiative losses, based on comparing the atomic contribution of $H\alpha$ with the total measured $H\alpha$, which only depends on the atomic analysis part of the analysis and should be generally applicable to other devices.

Although there are no strict n_e, T_e limits of this analysis, a 'soft' validity regime is estimated at $n_e = [10^{19}–5 \times 10^{20}]$ m^{-3} (based on Stark broadening inferences and photon opacity—more information will follow) and $T_e = [0.2–50]$ eV (based on the availability of collisional-radiative model data [27, 23].

For the most part, based on the synthetic testing result, we would expect also the full analysis chain to be fairly well applicable also to other devices, given some caveats.

Since the total $H\alpha$ emission in the divertor associated with plasma–molecule interactions (photons s^{-1}) is sufficient for quantitatively estimating MAR ion sinks and radiative power losses associated with H_2 chemistry, those two analysis estimates are robust against chordal integration effects, which is in agreement with the synthetic testing results. The separation between emission from H_2^+ and H^- could be more sensitive to chordal integration effects, given its relatively strong dependence on the electron density (figure 5). Chordal integration effects could occur as the Stark-broadened n_e estimate from the higher-n Balmer lines (which are more sensitive to EIR) could be different from the electron density at the H_2^+ and H^- emission location (see for example figures 10(d) and (j)); although this was not found to lead to a discrepancy in the synthetic testing results. MAI estimates from the BaSPMI are more sensitive to chordal integral effects, given the strong temperature dependence of the MAI per $H\alpha$ ratio (figure 18). This is also shown in the synthetic testing results in section 3.

This analysis relies on the lower-n Balmer lines and as such is susceptible to opacity. Photon opacity occurs at high neutral densities which are often correlated with high electron densities. In devices where $Ly\beta$ opacity is significant, which can be monitored using VUV spectroscopy based on the measured $Ly\beta/H\alpha$ ratio, such as JET [11] and C-Mod [20], modifications to this analysis have to be employed to separate the $H\alpha$ increase due to molecular processes and due to opacity.

5.6.2. Applicability in terms of viewing geometry. One caveat to the general applicability of the atomic Balmer line analysis (and thus also BaSMPI), is the placement of the lines of sight [5]. If the lines of sight are placed in such a way that they go through both a significant ionisation and bright recombination emission region, the electron-impact excitation contribution to the total Balmer line emission could be lower than a few percent. In that case, there is insufficient information about electron-impact excitation in the signal resulting in large uncertainties in the ionisation estimates. This can occur if there is a large shift between the respective electron densities and electron temperature profiles along the line of sight [52].

It should be noted, however, that a closed and higher density divertor may also facilitate a more natural separation of

the various emission regions as the characteristics mean-free-paths become smaller. This, for instance, is why the synthetic testing results are more consistent for MAST-U than TCV (see section 3).

5.6.3. Applicability in terms of diagnostic capabilities. As illustrated in this work, inferring information from plasma–molecule interactions simultaneously with the ionisation source complicates extracting the ionisation rate in strongly detached conditions unless temperature 'constraints' are employed. Although the temperature constraints employed here may only be applicable to specific situations or specific devices, other constraints could be employed, for instance based on divertor Thomson scattering or impurity line spectroscopy. Essentially, what is required is a way of estimating whether the inferred electron-impact excitation temperature (T_e^E) for a single (or multiple) chord(s) is 'likely' or 'unlikely'. T_e^E will correspond to the characteristic temperature of the high temperature region along the line of sight. Those temperature constraints enable obtaining ionisation estimates even when the electron-impact excitation (of H) component of the Balmer line emission is fairly small.

The full BaSPMI analysis puts requirements on the used divertor spectroscopy system. It requires inferred electron densities (from Stark broadening for line-of-sight spectroscopy—$n_e > 10^{19}$ m^{-3} [25]) as well as high quality absolute brightness of two medium-n Balmer lines in addition to $H\alpha$ and $H\beta$. Therefore, BaSPMI requires a flexible spectroscopy system which can be used to measure 4–5 Balmer lines. Given the large differences between the brightnesses of the various Balmer lines, these measurements may likely have to be restricted to measuring 1–2 Balmer lines at the same time. In that case, either repeat discharges or multiple spectrometers would be required to measure the 4–5 required Balmer lines. Neutral density filters may need to be employed to attenuate the emission of the particularly bright Balmer lines ($H\alpha$, $H\beta$).

Ultimately, the entire analysis technique can be improved through the inclusion of multiple diagnostics in a consistent statistical framework such as in [50]. Such a technique would use '2D spectroscopy' using filtered camera imaging [40]. This could be further improved by complementing the Balmer line measurements with impurity lines, such as He-I lines, providing more information on electron temperature and electron density (see discussion in section 5.4). Using toroidally-view filtered camera imaging spectroscopy would also enable a more precise localisation of all the different processes involved both along and across the field lines. This (partially) resolves the difficulty of 'line integration' effects and facilitates the separation of the various processes—since they are already spatially separated [35]. Additionally, such a 2D variety of the analysis could enable estimating 2D maps of the H_2^+ and H^- densities, which is not feasible otherwise.

6. Summary

Both plasma-atom and H_2 plasma chemistry (involving H_2^+ and/or H^-) can result in excited atoms leading to hydrogen atomic line emission. We have developed a new quantitative analysis technique, BaSPMI, to separate the emission of all Balmer lines into their electron-impact excitation (of H), EIR (of H^+) and H_2 plasma chemistry related (involving H_2, H_2^+, H^-) contributions. This is facilitated using the consistency between the medium-n ($H\gamma, H\delta$) Balmer lines, which are less sensitive to plasma–molecule interactions, and lower-n Balmer lines ($H\alpha, H\beta$). The individual emission contributions are then used to:

- Estimate the particle sources/sinks through plasma-atom (ionisation, recombination) and plasma-molecule (MAR/MAI) interactions.
- Estimate the radiative loss from *excited atoms* arising from plasma-atom and plasma–molecule interactions.

This analysis technique is validated by analysing synthetic spectra obtained from a synthetic divertor spectrometer using SOLPS simulations of both TCV and MAST-U. The Balmer line emissivity profiles along each line of sight showed strong spatial variations depending on the type of plasma-atom/molecule interaction. Despite this, however, the analysis result was in fair agreement (e.g. within uncertainty) with the direct outputs from SOLPS-ITER. The analysis was further tested by artificially removing certain plasma-atom/molecule interaction processes from the synthetic brightness. In this additional testing, the analysis correctly pointed out the lack of the removed processes.

The analysis makes several assumptions which have been discussed in detail. It has been shown that these have only minor impacts on the analysis result. In particular, we have shown that the MAR ion sink in the plasma can be readily estimated by comparing the expected atomic contribution of $H\alpha$ (based on only the analysis of a medium-n ($n = 5, 6, 7$) Balmer line pair) to the measured $H\alpha$. Those simplified MAR estimates are in quantitative agreement to the MAR estimates of the full BaSPMI result. The full BaSPMI analysis is, however, required to separate the contributions of H_2^+ and H^- to the Balmer line emission as well as to estimate the impact of H_2 plasma chemistry on the medium-n Balmer lines.

An experimental illustration of the analysis on TCV has been presented, indicating that plasma–molecule interactions can significantly contribute to the Balmer line emission. This has important implications for the diagnosis of tokamak divertors using hydrogen atomic line spectroscopy. We believe that this analysis technique should be generally applicable (in conditions where there is no significant photon opacity) to other tokamak devices to address those implications.

$$
\begin{aligned}
B_{n\to2}^{H_2,H_2^+,H^-} &\approx \underbrace{\Delta L n_e n_{H_2} PEC_{n\to2}^{H_2}(n_e,T_e)}_{B_{n\to2}^{H_2}} + \underbrace{\Delta L n_e n_{H_2^+} PEC_{n\to2}^{H_2^+}(n_e,T_e)}_{B_{n\to2}^{H_2^+}} \\
&\quad + \underbrace{\Delta L n_e n_{H^-} PEC_{n\to2}^{H^-+H^+}(n_e,T_e)}_{B_{n\to2}^{H^-}}.
\end{aligned} \tag{A2}
$$

Appendix A. Balmer line emission model description for plasma–molecule interactions

Balmer line emission attributed to H_2 plasma chemistry can arise from interactions with H_2, H_2^+, H_3^+ and H^- (figure 1). In addition, Balmer line emission associated with H^- can arise from either reactions starting with $H^- + H_2^+$ or $H^- + H^+$. Using a slab model for the plasma, we can describe the Balmer line brightness associated with H_2 chemistry ($B_{n\to2}^{H_2,H_2^+,H^-}$ — photons m^{-2} s) using equation (A1). Such plasma-slab models assume that all processes occur at the same location physically and implications of this have been discussed in detail for atomic reactions in literature [5, 9, 10, 25].

The PEC coefficients in equation (A1), obtained through Yacora (on the Web) [22, 23], are functions of the electron density, electron temperature, as well as the temperatures of the molecular species (H_2, H_2^+, H_3^+, H^-). Those latter temperature dependencies have, however, been found to be insignificant ($\ll 1\%$) for most pathways (except H^-[14]) and thus a 1 eV temperature for H_2, H_2^+, H_3^+ has been assumed.

$$
\begin{aligned}
B_{n\to2}^{H_2,H_2^+,H^-} &= \Delta L n_e n_{H_2} PEC_{n\to2}^{H_2}(n_e,T_e) \\
&\quad + \Delta L n_e n_{H_2^+} PEC_{n\to2}^{H_2^+}(n_e,T_e) \\
&\quad + \Delta L n_e n_{H_3^+} PEC_{n\to2}^{H_3^+}(n_e,T_e) \\
&\quad + \Delta L n_{H^+} n_{H^-} PEC_{n\to2}^{H^-+H^+}(n_e,T_e,T_{H^+},T_{H^-}) \\
&\quad + \Delta L n_{H_2^+} n_{H^-} PEC_{n\to2}^{H^-+H_2^+}(n_e,T_e,T_{H_2^+},T_{H^-}).
\end{aligned} \tag{A1}
$$

To further simplify equation (A1), we ignore the emission contribution from H_3^+ (which we estimate to be negligible based on post-processing of SOLPS simulations—section 3) and we assume that all emission from H^- occurs from H^- interacting with H^+ (rather than H_2^+) as the H^+ density is far larger than the H_2^+ density while their PECs are similar at the region where we would expect emission from such processes to occur. With those simplifications, we now obtain equation (A2) for $B_{n\to2}^{H_2,H_2^+,H^-}$.

Appendix B. Detailed information on the iterative scheme and convergence

The analysis scheme uses an Euler iterative scheme in order to obtain self-consistent results between the various atomic and molecular contributions of the Balmer lines. The convergence of this *relative change* in the estimated molecular contribution to the medium-n Balmer line is tracked per each iteration until it is 'converged'. The convergence criteria for this are listed below and are applied to the *statistical output sample* (which is determined from all the various input distributions) for this relative change:

(a) At least 16% of the output sample should have a *negative* change in the estimated molecular contribution (to make sure the analysis result is not 'drifting' towards a positive change).
(b) At least 16% of the output sample should have a *positive* change in the estimated molecular contribution (to make sure the analysis result is not 'drifting' towards a positive change).
(c) The median of the change of the output sample should be between −0.2% and +0.2% (assuming the median is a proxy for the maximum likelihood, this makes sure that the analysis estimates are converged).
(d) 68% of the output sample should have a relative absolute change below 2% (assuming the equal-tailed 68% quantile [54] is a proxy for the highest density interval [54] confidence intervals, this makes sure that the estimated uncertainties are converged).

These convergence criteria have to be obeyed for at least four iterations simultaneously. These settings have been made after verifying that the results and their uncertainty have converged before reaching these criteria while keeping the number of iterations required acceptable (usually between 7 and 20).

Appendix C. Improving the analysis through temperature constraints

We introduce here two possible temperature constraints which can improve the analysis output estimates: one based on the excitation temperature near the target and one based on the observation of the CIII front. The goal of these 'constraints' is to provide some 'probability' for having a certain temperature at a certain location of the divertor. Other temperature constraints could be employed in a similar fashion. Before introducing our constraints, first we will explain how they are employed in the analysis technically.

---

[14] The additional temperature dependencies for H^- are similar for all transitions: $PEC_{n\to2}^{H^-+H^+} \approx f(T_{H^+},T_{H^-}) \times g(n,n_e,T_e)$ and therefore only impact the 'MAR/$H\alpha$ emission coefficient' ratios employed in section 2.5.2 in the analysis. A random temperature between 0.5 and 3 eV is assumed for the H^- temperature as it can get some of the Franck–Cordon energy of the H_2 bond (2.2 eV) when H_2 dissociatively attaches with an electron to form H^- ($e^- + H_2 \to H^- + H$). A random value between 0.8 and 1.5 times T_e^E is assumed for the H^+ temperature, as estimated from SOLPS-ITER simulations [37, 42, 53].

Each Monte Carlo output sample point contains an estimate for the excitation-derived temperature T_e^E. Given these constraints, we can compute the probability of that sample point being true (for this we assume an asymmetric Gaussian probability distribution for T_e^E). The samples and their probabilities are then mapped to a PDFs using a *weighted* Gaussian Kernel density estimator (as opposed to an adaptive *non-weighted* one when no constraints are employed [55]). From the PDF estimates, the maximum likelihood and shortest interval corresponding to 68% uncertainty can be extracted, representing the estimated outputs and its uncertainty in a similar way as done in [10].

This way of implementing constraints also changes how the integrated values should be obtained. Since the uncertainties are assumed to be systematic, the uncertainties applied to each chord per sample are the same—there is thus a correlation between the uncertainties of different chords when calculating integrated values (such as the total ionisation source). This could interfere with the way the constraints are built up. For instance, if all the analysis outputs would, hypothetically, be isothermal, then the maximum likelihood values of the temperature profile along the divertor leg would, after applying the constraints, not be isothermal (since a probability per point on the poloidal profile is ascribed). However, the integrated ionisation values would be determined all from isothermal solutions (since in this case a probability per poloidal profile is ascribed rather than a probability per point on the poloidal profile). Given these technicalities, we therefore determine the maximum likelihood of the poloidal profiles with their 68% confidence intervals of ionisation, recombination, etc and integrate these profiles (and their upper/lower estimates) to get the estimates for the integrated (ionisation source, recombination sink, etc parameters); which is more consistent with applying the constraints per point on the poloidal profile.

One drawback of the employed constraints is that it strongly reduces the 'effective' Monte Carlo sample size of the simulation (since many sample points are given low probabilities and are thus 'effectively excluded'). Therefore, the analysis would require a larger number of Monte Carlo samples and thus more computational time when such constraints are employed. Furthermore, the requirement of using a weighted Kernel density estimator makes the choice for a suitable Kernel density estimator more restricted.

Employing temperature constraints in the analysis is only necessary for electron-impact excitation (of H) derived quantities in detached conditions. Adding the constraints to the other quantities, however, changes the maximum likelihoods insignificantly, although it does reduce their uncertainties.

C.1. Target temperature constraint

Assuming that we have a estimate for a range of possible target temperatures, we can use this to constrain the analysis. In this, we assume that this target temperature estimate is similar to the excitation emission weighted temperature of the nearest chord at the target (T_t^E). For synthetic testing we obtain this estimate directly from the SOLPS output (assuming an uncertainty of

± 1 eV), while for the experimental analysis the target temperature has been estimated using power balance using the result from [5].

C.2. CIII temperature 'exclusion' constraints

An additional temperature constraint can be employed along the viewing chord fan; rather than a single point at the target. The front of the CIII (465 nm) emission line is an emission line frequently used in the qualitative characterisation of edge physics experiments in carbon devices, especially at TCV [39, 56, 57] where it is used as a 'proxy' for the 'cold front' taking off the target [57] during detachment experiments. Depending on transport, the expected temperature of such a 'front (1/e fall-off point)' (assuming the carbon concentration does not change dramatically over the field line) is 4–8 eV. Below the CIII front the electron temperature will likely not be hotter than 8 eV. Likewise, above the front, the temperature will likely not be colder than 4 eV: the CIII emission front thus provides us with information to spatially 'exclude' (e.g. lower the likeliness of) certain temperatures. We can thus constrain the temperature samples further by adding a probability function which represents this argument—equation (C1).

In here z represents the z position of the line of sight intersecting the divertor leg, z_f represents the CIII front location estimate and $T_{f,l}, T_{f,h}$ corresponds to the lowest/highest-temperature estimate of the front respectively. In this case, z_f is determined analogously to [56, 57] as the 1/e fall-off-length of the CIII emission profile, which is determined by line of sight spectroscopy. The probability used for each line of sight shown in equation (C1) represents an analytical depiction of the multiplication of two block-functions making two clauses likely: below CIII front z_f and below temperature $T_{f,h} = 8$ eV & above CIII front z_f and above temperature $T_{f,l} = 4$ eV. The fall-off length of the functions are set to $k_z = 2$ cm and $k_T = 1.5$ eV respectively. The solutions are largely insensitive to relatively modest changes of these fall-off parameters and temperature points.

$$P(T_e) = \frac{1}{1 + \exp\left(\frac{z_f - z}{k_z}\right)} \frac{1}{1 + \exp\left(\frac{T_{f,l} - T_e}{k_T}\right)}$$
$$+ \left[1 - \frac{1}{1 + \exp\left(\frac{z_f - z}{k_z}\right)}\right]\left[1 - \frac{1}{1 + \exp\left(\frac{T_{f,h} - T_e}{k_T}\right)}\right].$$
$$\text{(C1)}$$

ORCID iDs

K Verhaegh ⓘ https://orcid.org/0000-0002-0500-2764
B Lipschultz ⓘ https://orcid.org/0000-0001-5968-3684
C Bowman ⓘ https://orcid.org/0000-0002-0813-2206
U Fantz ⓘ https://orcid.org/0000-0003-2239-3477
A Fil ⓘ https://orcid.org/0000-0001-5755-4440
J R Harrison ⓘ https://orcid.org/0000-0003-2906-5097
D Wünderlich ⓘ https://orcid.org/0000-0003-2810-9633
D S Gahle ⓘ https://orcid.org/0000-0002-4434-7626

A Perek ![ORCID] https://orcid.org/0000-0002-4117-0298
M Wensing ![ORCID] https://orcid.org/0000-0003-4462-7860

References

[1] Pitts R A *et al* 2013 *J. Nucl. Mater.* **438** S48–S56
[2] Loarte A *et al* 2007 *Nucl. Fusion* **47** S203–S263
[3] Pitcher C S and Stangeby P C 1997 *Plasma Phys. Control. Fusion* **39** 779–930
[4] Stangeby P C 2018 *Plasma Phys. Control. Fusion* **60** 044022
[5] Verhaegh K *et al* 2019 *Nucl. Fusion* **59** 126038
[6] Krasheninnikov S I and Kukushkin A S 2017 *J. Plasma Phys.* **83** 155830501
[7] Terry J L, Lipschultz B, Bonnin X, Boswell C, Krasheninnikov S I, Pigarov A Y, LaBombard B, Pappas D A and Scott H A 1999 *J. Nucl. Mater.* **266–9** 30–6
[8] Lipschultz B, Terry J L, Boswell C, Hubbard A, LaBombard B and Pappas D A 1998 *Phys. Rev. Lett.* **81** 1007–10
[9] Verhaegh K *et al* 2017 *Nucl. Mater. Energy* **12** 1112–17
[10] Verhaegh K, Lipschultz B, Duval B, Fil A, Wensing M, Bowman C and Gahle D 2019 *Plasma Phys. Control. Fusion* **61** 125018
[11] Lomanowski B, Groth M, Coffey I H, Karhunen J, Maggi C F, Meigs A, Menmuir S and O'Mullane M 2020 *Plasma Phys. Control. Fusion* **62** 065006
[12] Krasheninnikov S, Pigarov A Y, Knoll D, LaBombard B, Lipschultz B, Sigmar D, Soboleva T, Terry J and Wising F 1997 *Phys. Plasmas* **4** 1638–46
[13] Fantz U 2002 *Contrib. Plasma Phys.* **42** 675–84
[14] Fantz U, Reiter D, Heger B and Coster D 2001 *J. Nucl. Mater.* **290** 367–73
[15] Sakamoto M *et al* 2017 *Nucl. Mater. Energy* **12** 1004–9
[16] Hollmann E M, Brezinsek S, Brooks N H, Groth M, McLean A G, Pigarov A Y and Rudakov D L 2006 *Plasma Phys. Control. Fusion* **48** 1165
[17] Groth M *et al* 2019 *Nucl. Mater. Energy* **19** 211–17
[18] Kukushkin A S, Krasheninnikov S I, Pshenov A A and Reiter D 2017 *Nucl. Mater. Energy* **12** 984–8
[19] Wischmeier M *et al* 2004 *Contrib. Plasma Phys.* **44** 268–73
[20] Terry J L, Lipschultz B, Pigarov A Y, Krasheninnikov S I, LaBombard B, Lumma D, Ohkawa H, Pappas D and Umansky M 1998 *Phys. Plasmas* **5** 1759–66
[21] Terakado A *et al* 2019 *Nucl. Mater. Energy* **20** 100679
[22] Wünderlich D and Fantz U 2016 *Atoms* **4** 26
[23] Wünderlich D, Giacomin M, Ritz R and Fantz U 2020 *J. Quant. Spectrosc. Radiat. Transfer* **240** 106695
[24] Verhaegh K *et al Nucl. Mater. Energy* submitted (https://arxiv.org/abs/2008.00272)
[25] Verhaegh K 2018 Spectroscopic investigations of detachment on TCV Thesis (available at: http://etheses.whiterose.ac.uk/22523/)
[26] Summers H P, Dickson W J, O'Mullane M G, Badnell N R, Whiteford A D, Brooks D H, Lang J, Loch S D and Griffin D C 2006 *Plasma Phys. Control. Fusion* **48** 263–93
[27] O'Mullane M 2013 Adas: Generalised collisonal radiative data for hydrogen *Technical Report* (available at: www.adas.ac.uk)
[28] Hinkley D V 1969 *Biometrika* **56** 635–9
[29] Kotov V, Reiter D and Kukushkin A S 2007 Numerical study of the ITER divertor plasma with the B2-Eirene code package (https://inis.iaea.org/search/search.aspx?orig_q=RN:39025830)
[30] Reiter D *et al* 2008 The Eirene code user manual Report Forschungszentrum Jülich GmbH (available at: www.eirene.de/manuals/eirene.pdf)
[31] Reiter D, Baelmans M and Börner P 2005 *Fusion Sci. Technol.* **47** 172–86
[32] Stangeby P C and Chaofeng S 2017 *Nucl. Fusion* **57** 056007
[33] McLean A 2019 Understanding plasma divertor detachment in fusion power reactors *Technical Report* (Livermore, CA, United States: Lawrence Livermore National Lab. (LLNL)) (https://doi.org/10.2172/1573451)
[34] Sawada K and Fujimoto T 1995 *J. Appl. Phys.* **78** 2913–24
[35] Perek A *et al* 2019 *Rev. Sci. Instrum.* **90** 123514
[36] Kukushkin A and Pacher H 2016 *Contrib. Plasma Phys.* **56** 711–16
[37] Fil A M D, Dudson B D, Lipschultz B, Moulton D, Verhaegh K H A, Fevrier O and Wensing M 2017 *Contrib. Plasma Phys.* **58** 746–750
[38] Myatra O, Moulton D, Fil A, Dudson B and Lipschultz B 2018 Taming the flame: detachment access and control in MAST-U Super-X *Plasma Surface Interactions* (*Princeton, US, 18-22 June 2018, Princeton, US*) (https://fusion-cdt.ac.uk/wp-content/uploads/2018/08/Myatra-Omkar-psi_poster.pdf)
[39] Ravensbergen T *et al* 2020 *Nucl. Fusion* **60** 066017
[40] Perek A *et al* 2020 *Nucl. Mater. Energy* **26** 100858
[41] Brezinsek S, Sergienko G, Pospieszczyk A, Mertens P, Samm U and Greenland P T 2005 *Plasma Phys. Control. Fusion* **47** 615–34
[42] Fil A, Lipschultz B, Moulton D, Dudson B D, Février O, Myatra O, Theiler C, Verhaegh K and Wensing M 2020 *Plasma Phys. Control. Fusion* **62** 035008
[43] Shirai T, Tabata T, Tawara H and Itikawa Y 2002 *At. Data Nucl. Data Tables* **80** 147–204
[44] Behringer K and Fantz U 2000 *New J. Phys.* **2** 23
[45] Stangeby P 2000 *The Plasma Boundary of Magnetic Fusion Devices. Series: Series in Plasma Physics* vol 7, ed P Stangeby (London: Taylor and Francis)
[46] Wischmeier M 2005 Simulating divertor detachment in the TCV and JET tokamaks Thesis (https://doi.org/10.5075/epfl-thesis-3176)
[47] Cadez I, Markelj S and Milosavljevic A R 2011 *Nucl. Eng. Des.* **241** 1267–71 Conf. on Nuclear Energy for New Europe 2019
[48] Miyamoto K, Hatayama A, Ishii Y, Miyamoto T and Fukano A 2003 *J. Nucl. Mater.* **313–6** 1036–40
[49] Lisgo S, Borner P, Counsell G F, Dowling J, Kirk A, Scannell R, O'Mullane M, Reiter D and Team M 2009 *J. Nucl. Mater.* **390–1** 1078–80
[50] Bowman C, Harrison J R, Lipschultz B, Orchard S, Gibson K J, Carr M, Verhaegh K and Myatra O 2020 *Plasma Phys. Control. Fusion* **62** 045014
[51] Krishnakumar E, Denifl S, Čadež I, Markelj S and Mason N J 2011 *Phys. Rev. Lett.* **106** 243201
[52] Reimold F *et al* 2017 *Nucl. Mater. Energy* **12** 193–9
[53] Wensing M *et al* 2019 *Plasma Phys. Control. Fusion* **61** 085029
[54] Cowles M K 2013 *Applied Bayesian Statistics: With R and Openbugs Examples* vol 98 (New York: Springer Science & Business Media)
[55] Botev Z I, Grotowski J F and Kroese D P 2010 *Ann. Stat.* **38** 2916–57
[56] Theiler C *et al* 2017 *Nucl. Fusion* **57** 072008
[57] Harrison J R *et al* 2017 *Nucl. Mater. Energy* **12** 1071–6